Journal of Volcanology and Geothermal Research 471 (2026) 108535

Contents lists available at ScienceDirect

Journal of Volcanology and Geothermal Research

journal homepage: www.journals.elsevier.com/journal-of-volcanology-and-geothermal-research

Hyperspectral imaging, mineralogy, and degassing: Exploring the volcanic hydrothermal system of Red Crater, Tongariro, Aotearoa New Zealand

Daniel Sturgess [a,*], Gabor Kereszturi [a], Agnes Mazot [b], Rachelle Sanchez [a], Antonio M. Álvarez-Valero [c], Vladyslav Zakharovskyi [a]

[a] Volcanic Risk Solutions, School of Agriculture and Environment, Massey University, Palmerston North, New Zealand
[b] Earth Sciences New Zealand, Wairakei Research Centre, Taupō, New Zealand
[c] Department of Geology, University of Salamanca, Salamanca, Spain

ARTICLE INFO

Keywords:
Hyperspectral imaging
Imaging spectroscopy
Hydrothermal alteration
Volcano mapping
Degassing
Geochemistry

ABSTRACT

Hydrothermal alteration on volcanoes can compromise the strength and permeability of the host rock, contributing to flank collapses (e.g., Te Maari, 2012) and phreatic eruptions (e.g., Whakaari, 2019). Alteration processes occur at volcanoes hosting hydrothermal systems, where hot, acidic fluid flow is driven by a supply of magmatic heat and gas inputs, resulting in the dissolution of primary minerals and the deposition of secondary assemblages. We investigated hydrothermal alteration at Red Crater, Tongariro, Aotearoa New Zealand, using a combination of laboratory and airborne hyperspectral imaging, mineralogical, and geochemical techniques. Two distinct alteration styles were identified: (1) advanced argillic alteration, characterised by amorphous silica, kaolinite, and alunite, primarily focused at the Red Crater scoria cone, and (2) silicification at Oturere and the Emerald Lakes. The distribution of these units was mapped using supervised image classification of airborne hyperspectral data. Textural and isotopic analyses suggest acid-sulphate alteration is primarily driven by the oxidation of rising H_2S in a steam-heated environment. Red Crater hosts four main regions of heightened degassing, coinciding with geothermal surface features and hydrothermal alteration deposits, with 26.2 ±1.5 t/d of CO_2 emissions and an H_2S flux of 131.1 g/m^2/d. This study presents a conceptual model of hydrothermal alteration processes at Red Crater. Our mapping of alteration and degassing can indicate areas of potential future hazards, and may support simulations assessing flank instability, improving hazard assessment at this active vent.

1. Introduction

Volcanic hydrothermal systems evolve as hot magmatic fluids interact with meteoric/oceanic water that infiltrates the volcano's edifice (Aizawa et al., 2009). Hot fluid flow in these shallow zones is driven by a supply of magmatic heat and gas inputs to the system from shallow intrusion complexes and magma bodies (Giggenbach, 1997). Over time, hydrothermal fluids infiltrate pore spaces, leading to the alteration of host rocks, whereby the primary mineralogy can be dissolved and replaced by new minerals in equilibrium with the environment (Browne, 1978; McCollom and Shock, 1998). These complex processes are chiefly controlled by the host rock's mineralogy and permeability, combined with the temperature, pH, fluid–rock ratio, and fluid chemistry of the system, leading to a large variety of replacement minerals (Schwartz, 1959). Particular alteration mineral assemblages can be diagnostic of the underlying processes within the hydrothermal system, and based on this, general classifications of alteration styles can be delineated as silicic (e.g., Fulignati and Sbrana, 1998; Potro and Hürlimann, 2009), argillic (intermediate/advanced) (e.g., Kereszturi et al., 2020), propylitic (e.g., Pacey et al., 2020), and phyllic (e.g., Pour and Hashim, 2012) (Table 1). Surface manifestations of volcanic hydrothermal systems include crater lakes, fumaroles, and hot springs, and studying their temperature and gas compositions provides insights into the conditions of the system (Taran et al., 2000; Miller et al., 2018, 2020). Hydrothermal alteration can cause volcanic edifice instability and collapse due to a decrease in rock strength and low-permeability induced heightened pore-fluid pressures (Ball et al., 2018; Heap et al., 2020; Kereszturi et al., 2023). Indeed, alteration induced weakening of host rock has been identified as a contributing factor for multiple collapse events at Mount Ruapehu (Lecointre et al., 1998; Donoghue and Neall, 2001; Keigler et al., 2011; Tost et al., 2014; Kereszturi et al., 2021) and Tongariro (Topping, 1974; Lecointre et al., 2002; Procter et al., 2014). Volcanoes hosting hydrothermal systems are also prone

* Corresponding author.
E-mail address: d.sturgess@massey.ac.nz (D. Sturgess).

https://doi.org/10.1016/j.jvolgeores.2026.108535
Received 16 October 2025; Received in revised form 13 January 2026; Accepted 14 January 2026
Available online 15 January 2026

Table 1
Hydrothermal alteration styles, their approximate pH and temperature conditions, and a non-exhaustive list of common mineral associations (broadly following classifications and examples within Stoffregen (1987), Pirajno (1992), Hedenquist (2000), John et al. (2019), Fulignati (2020), Douglas et al. (2022)).

Alteration style	Temperature	pH	Mineral associations
Silicic	>100 °C	1–7	Quartz, opal-TC, cristobalite, pyrite
Propylitic	>220 °C	5.5–7	Chlorite, carbonates, pyrite, chalcopyrite, sericite, hematite, smectites, anhydrite
Phyllic	160–230 °C	5.5–7	Quartz, sericite, pyrite, illite, chlorite, hematite, anhydrite, carbonates
Argillic	<160 °C	5–7	Smectites, illite, kaolinite/halloysite/dickite, chlorite, sericite
Intermediate Argillic	<160 °C	4–6	Smectites, illite, kaolinite, chlorite
Advanced Argillic	<160–300 °C	2–4	Alunite, kaolinite/dickite, quartz, pyrite, jarosite

to phreatic eruptions (e.g., Te Maari, 2012; Pardo et al., 2014 and Whakaari, 2019; Dempsey et al., 2020). Phreatic events are generated by the sudden flashing of water into steam when heated by an intruding magma body or volatiles, or when steam expands due to significant pressure changes via flank collapse or conduit sealing (Procter et al., 2014; Montanaro et al., 2022).

Point-based and imaging hyperspectral remote sensing is a valuable tool used to identify, quantify, and map alteration minerals at laboratory, airborne, and satellite scales (Crósta et al., 1998; Kereszturi et al., 2020; Corrado et al., 2025; Thiele et al., 2025). Hyperspectral sensors capture the electromagnetic radiation emitted or reflected by an object using hundreds of contiguous and overlapping channels comprised of wavelengths on the electromagnetic spectrum (Goetz, 2009; Plaza et al., 2009). Typical sensors used for alteration mapping cover the Visible to Near-Infrared (VNIR 350–1000 nm) and Shortwave-Infrared (SWIR 1000–2500 nm) regions (Plaza et al., 2009), however, others utilise Mid-Infrared (MIR 3000–5000 nm) and Long-Wave Infrared (LWIR 7500–14,000 nm) also (van der Meer et al., 2012; Kumar and Ghosh, 2017; Feng et al., 2018). Individual minerals can be identified based on diagnostic absorption features present within the spectra. The position, width, and depth of such absorption features are controlled by chemical bonds, vibrational processes, and electronic transitions within the mineral's crystal lattice (Clark et al., 1990; Douglas et al., 2022). Hyperspectral imaging provides an efficient and non-destructive tool for studying alteration.

This study investigates hydrothermal alteration at Red Crater, Tongariro, Aotearoa New Zealand, using a combination of laboratory and airborne hyperspectral, mineralogical, and geochemical techniques. Tongariro's geological evolution has been well studied (Pure et al., 2020; Leonard et al., 2021); however, comprehensive surface alteration mineralogy data for the volcano are limited. Studying hydrothermal alteration can improve our understanding of degassing processes and volcanic evolution, support the development of a conceptual model of the system, and ultimately inform assessments of hazards associated with hydrothermal activity.

1.1. Geological background

Red Crater (39° 08'11.4"S 175° 39'04.4"E, 1886 m), so named because of its distinctive oxidised deposits, is an active vent of the ~350 ky Tongariro volcano (Pure et al., 2023). Tongariro is situated at the southern end of the Taupō Volcanic Zone (TVZ), a 300 × 60 km wide active volcano-tectonic region in the centre of New Zealand's North Island, generated by the westward subduction of the Pacific Plate beneath the Australian Plate (Wilson et al., 1995). The massif consists of medium-K basaltic-andesite to dacite eruptive products from multiple vents and magma systems that have been concurrently active throughout its history (Scott and Potter, 2014; Pure et al., 2023). Red Crater is positioned upon the head of the glacially eroded Oturere Valley and comprises a basaltic-andesite scoria cone, enclosing an unusually well-preserved dyke (Bardsley, 2004; Wadsworth et al., 2015). The site also includes multiple ancillary phreatic/phreatomagmatic explosion craters, three of which are occupied by Ngā Rotopounamu/Emerald Lakes (Shane et al., 2017), which are surrounded by a regolith composed of undifferentiated late Quaternary and Holocene tephra, fan and scree deposits (Fig. 1).

The vent is one of the youngest (~11 ka) on Tongariro, constructed of two eruptive members that overlie the ~96–79 ka Waitakatorua (*awu*) and ~79–61 ka Rotopaunga (*arp*) Members of the Taiko formation (Pure et al., 2020). The Te Ahititi (*ahi*) andesites (~11–1.8 ka) are the oldest and most voluminous products from Red Crater, characterised by lava flows into Oturere Valley (Hobden, 1997; Pure et al., 2020), the largest of which (~371–640 million m^3) travelled ~6.5 km (Stevens, 2002). The younger Te Rongo (*mtr*) basaltic-andesite (~1.8 ka–1800 CE) (Pure et al., 2020) deposits mark a shift in the magmatic composition of Red Crater's plumbing system around 1.8 ka from andesite (SiO_2 ~59–62 wt%) to basaltic-andesite (SiO_2 ~53–54 wt%) (Shane et al., 2017). This change was facilitated by sufficient draining of the pre-1.8 ka andesitic reservoir, allowing for subsequent mafic recharge via repeated intrusions. The primary mineralogical phases of Red Crater products are broadly similar between the two members, displaying a dominance of plagioclase and clinopyroxene phenocrysts with minor orthopyroxene, olivine and Fe-Ti oxides (Bardsley, 2004; Shane et al., 2017; Pure et al., 2020). Post-1.8 ka Te Rongo lava samples are however comparatively crystal-poor, and contain plagioclase phenocryst overgrowths with heightened FeO and MgO contents (Shane et al., 2017). Post-1.8 ka activity at Red Crater involved fire fountains and strombolian construction of the present day scoria cone (Bardsley, 2004) and 6 lava flows into South Crater, Central Crater (the most mafic end member composition on record from Tongariro), and Oturere Valley (Shane et al., 2017; Pure et al., 2020). Magma drain back from the active dyke and concurrent conclusion of this activity was followed by hydrothermally driven eruptions, forming the Emerald Lake craters, and excavating the aforementioned dyke and the North East Crater Wall of the scoria cone (Walsh et al., 1998; Bardsley, 2004; Wadsworth et al., 2015). Historically, at least 16 tephra dispersing eruptions have occurred from the vent in last ~300 years (Moebis et al., 2011). Several eruptions have been identified since 1855 (Scott and Potter, 2014), with the most recent thought to have occurred in 1934.

Geothermal activity at Red Crater consists of areas of hot steaming ground (≤100°C) and active fumaroles (≤109°C) located around the scoria cone, Oturere and the Emerald Lakes. Oturere is the largest and most active of these regions, characterised by tephra deposits overlying fractured and variably altered Waitakatorua lava (Fig. 2b). These geothermally active areas are surface expressions of Tongariro's vapour-dominated hydrothermal system, which extends from Ngāuruhoe's northern flank to Upper Te Maari (Walsh et al., 1998; Hill et al., 2015; Miller and Williams-Jones, 2016; Miller et al., 2018). The most recent eruptions at Tongariro were two hydrothermal events from Upper Te Maari in August and November 2012 (Scott and Potter, 2014).

Surface mapping of alteration products at Tongariro is limited, few studies have detailed specific minerals and their extents. Lecointre et al. (2002) identified alteration minerals including kaolinite, halloysite, and smectites at Ketetahi and, amorphous silica, natroalunite, and halloysite at the southern ridge of Tongariro. Cole et al. (2018) developed a geological map of South Crater and detailed hydrothermally altered

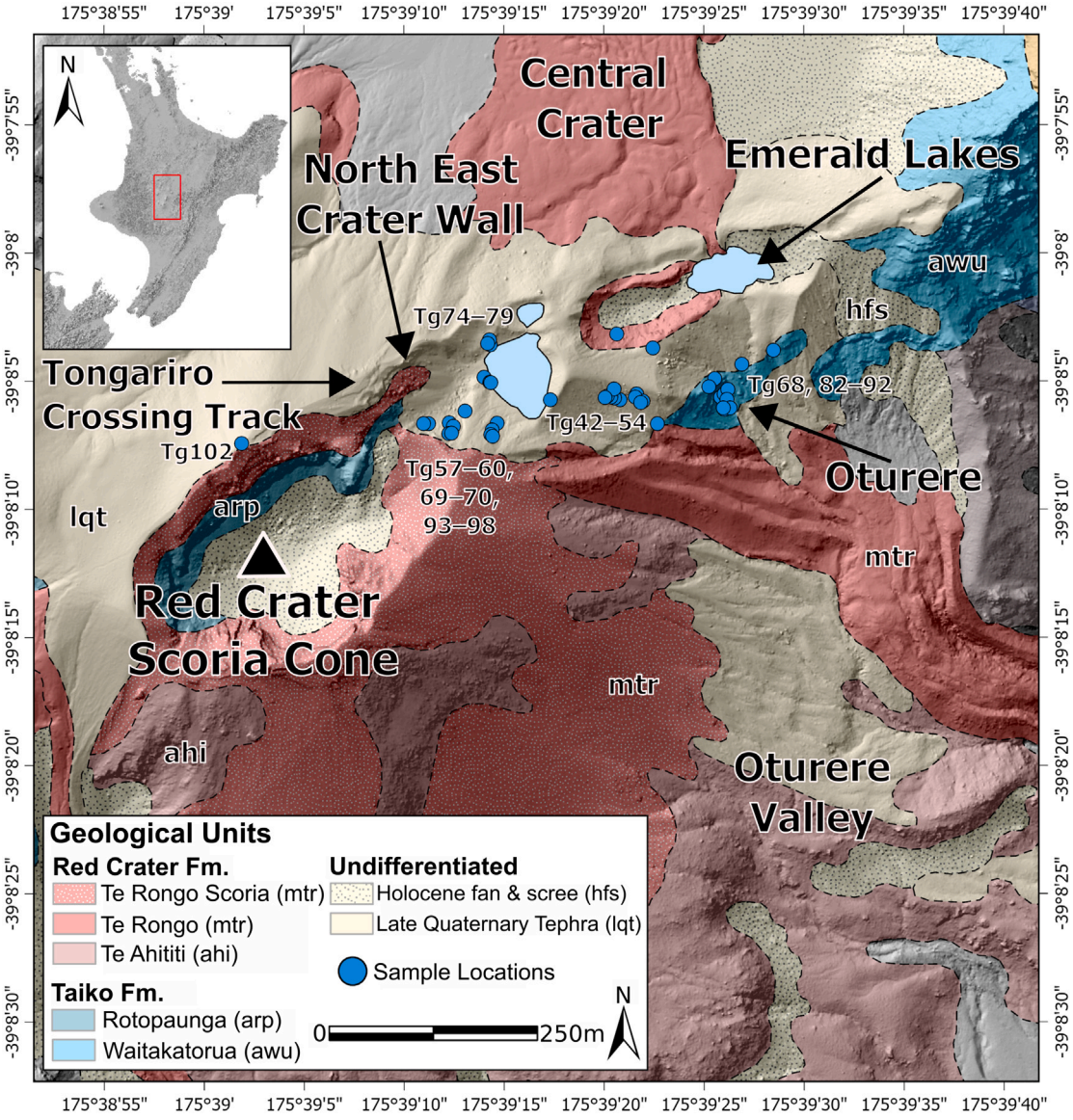

Fig. 1. Simplified geological map of the Red Crater area on Tongariro draped over a 1 m hillshade, displaying key regions of interest and the locations of samples used in this study. Geological formation abbreviations: mtr = Te Rongo, ahi = Te Ahititi, arp = Rotopaunga, awu = Waitakatorua (Pure et al., 2020), hfs = Holocene fan and scree, lqt = Late Quaternary tephra. New Zealand basemap and Tongariro 1 m hillshade from Land Information New Zealand, geological units and Emerald Lakes polygons from GNS Science web map service.

areas associated with glacial meltwaters and geothermal activity, identifying minerals including smectites, alunite, and Fe oxides. Kereszturi et al. (2018) mapped re-worked and in-situ alteration products, including montmorrillonite, kaolinite, and nontronite, at Te Maari after the 2012 eruptions. The total volume of hydrothermally altered material at Tongariro is estimated at ~20 km^3 and several steep slopes on the edifice coincide with altered rocks (Miller and Williams-Jones, 2016). Investigating alteration processes is necessary for hazard assessment and mitigation at Tongariro, as these areas may be prone to instability and collapse.

2. Methods

2.1. Field sampling and laboratory analysis

Multiple sampling campaigns between January 2024–March 2025 were conducted at Red Crater, from which a total of 45 samples were collected (Fig. 1, see supplementary material for full sample list). They range from non-altered, to moderately and pervasively altered tephra, scoria, blocks and lava.

2.2. Reflectance spectroscopy

Laboratory-based reflectance spectroscopy of the rim and interior of the samples in the VNIR and SWIR regions was conducted by taking spot based measurements using the ASD FieldSpec 4. We used a Spectralon white reference panel for calibration and, prior to spectroscopy, the samples were oven dried at 30°C for 48 h to minimise the influence of water absorption. Multiple spot measurements of the crust and interior were made using a high intensity contact probe with a spatial footprint of ~8 mm across, ensuring a representative dataset for each rock. At least 100 measurements were recorded for each spot, they were splice corrected to account for the step between the VNIR and SWIR sensors (Crucil et al., 2019), averaged, and then exported to create a spectral library of all samples. To identify specific minerals we used both reflectance and continuum removed spectra (e.g., Clark, 1999),

and manually matched absorption features (depth and position) with those in the United States Geological Survey (USGS) Spectral Library Version 7 (Kokaly et al., 2017).

2.3. Scanning electron microscopy and energy dispersive spectroscopy

Seven thick sections (100 μm) were prepared for geochemical and petrographic analysis via Energy Dispersive Spectroscopy (EDS) and Scanning Electron Microscopy (SEM). The samples were mounted on glass slides, ground to ~100 μm, polished to ~1 μm, gold coated and imaged using a JEOL JCM-6000 Plus SEM with an acceleration voltage of 15 kV and 10 mm working distance. Minerals were identified based on their crystal habit displayed in SEM images and elemental composition from EDS count spectra and mol% data.

2.4. Stable isotopes

Oxygen ($\delta^{18}O$) and sulphur ($\delta^{34}S$) stable isotope analyses were conducted on four native sulphur samples (Tg46–48, 54) and one alunite sample (Tg57b) (Table 5) using a VG-Isotech SIRA-II dual-inlet mass spectrometer. Samples were selected based on mineral identification from spectroscopy and SEM-EDS analyses.

Oxygen isotope values were measured from the SO_4^- site of the alunite sample, following methods from Rafter (1957), Rees and Holt (1991). Each sample was analysed three times, checked against reference standards NBS-127, IAEA-SO-5, and IAEA-SO-6, recording the $\delta^{18}O$ relative to Vienna Standard Mean Ocean Water (VSMOW) (Craig, 1961). Sulphur isotope values were measured from native sulphur crystals (or powdered as whole rock when unavailable) and the SO_4^- site of the alunite sample. The extraction (and conversion for sulphates) procedures of SO_2 differ for alunite and native sulphur, following Robinson and Kusakabe (1975), Yanagisawa and Sakai (1983), Wasserman et al. (1992), Manalo et al. (2018), Li et al. (2024), Imura et al. (2024), Álverez-Valero et al. (2025), Sanchez et al. (2025). Ratios are relative to the Canyon Diablo iron meteorite reference (troilite $^{34}S/^{32}S$ = 0.0450045) (Ault and Jensen, 1963).

2.5. Aerial hyperspectral survey and image classification

An airborne hyperspectral survey of Tongariro was conducted using a Piper PA-34-200 aircraft with the HySpex VNIR-1800 (400–1000 nm) and SWIR-384 (930–2500 nm) push-broom hyperspectral cameras between 1130 and 1300 NZDT (UTC +13) on 7th March 2025 (Table 2). The flight elevation was ~614 m above ground level, resulting in pixel resolutions of 0.6 m and 1.2 m for VNIR and SWIR images respectively. Each image strip was radiometrically corrected from Digital Numbers (DN) to at-sensor radiance ($W{\cdot}nm^{-1}{\cdot}sr^{-1}{\cdot}m^{-2}$) in HySpex RAD before atmospheric correction in ATCOR (Richter and Schläpfer, 2023). Geometric correction and orthorectification of images was performed using Applanix POSPac, HySpex NAV, and PARGE (Richter and Schläpfer, 2002), using a 1 m LiDAR Digital Elevation Model (DEM) from Land Information New Zealand. The strips were mosaicked together and spectra were smoothed using a Savitzky–Golay filter with a window size of 10 and 4 for VNIR and SWIR respectively. Finally, bands impaired by atmospheric interference were removed and Minimum Noise Fraction (MNF) (Green et al., 1988) was applied to the VNIR-SWIR layer stack to reduce the dimensionality of the data, discounting redundant and noisy spectral bands that may reduce image classification accuracy (Kereszturi et al., 2018). We retained 20 bands for the final hypercube based on manual thresholding using the Eigenvalue scree plot, maintaining variance based on the spectral signal and ensuring noise reduction, ready for image classification.

The spatial distribution of surface hydrothermal alteration at Red Crater was mapped using a supervised random forest image classification (Breiman, 2001). Random forests use multiple decision trees that each vote for a specific class to classify an input vector (i.e., image pixel), based on a set of user generated training data (Pal, 2005). We selected polygons labelled as one of the following six classes: silicic alteration, argillic alteration, lava, scoria, regolith, and shadow/water/steam, based on our field observations and sample mineralogy obtained from VNIR-SWIR laboratory spectroscopy and SEM-EDS data. These polygons were split 50–50 into training and validation data. The validation data are used to generate an error matrix and compute the accuracy of the classification using three metrics; overall accuracy, user's accuracy, and producer's accuracy (as defined by Congalton, 1991; Liu et al., 2007). The overall accuracy reports the percentage of correctly classified pixels from the entire independent validation dataset (Congalton, 1991). The user's accuracy measures the probability that a classified pixel from $class_i$ in the image correctly represents that class on the ground (Story and Congalton, 1986), while the producer's accuracy describes how many pixels in validation $class_i$ were correctly classified (Congalton, 1991). They are computed by the following equations:

$$\text{Overall Accuracy} = \frac{\text{total correct validation pixels}}{\text{total validation pixels}} \quad (1)$$

$$\text{User's Accuracy}_i = \frac{\text{total class}_i \text{ correct pixels}}{\text{total pixels in validation class}_i} \quad (2)$$

$$\text{Producer's Accuracy}_i = \frac{\text{total class}_i \text{ correct pixels}}{\text{total pixels classified as class}_i} \quad (3)$$

Model parameters were selected using a grid search method, which returned a maximum depth, minimum number of leaves (nodes) and a minimum number of splits of 15, 2, and 4 respectively, the number of trees were kept at 500. Each node within a tree uses a random selection of the square root of the total number of features (spectral bands) when split.

Table 2
Tongariro aerial hyperspectral survey parameters.

Parameter	Value
Date/Time	07/03/2025 1130–1300 NZDT (UTC +13)
Site Location	39° 08'11.4"S 175° 39'04.4"E
Flight Height	614 m agl
Spatial Resolution	VNIR: 0.6 m SWIR: 1.2 m
Full Width at Half Maximum	VNIR: 4.7 nm SWIR: 8.1 nm
Solar Elevation	51.7–54.2°
Solar Azimuth	34.2–23.9°
Solar Zenith	38.3–35.8°

2.6. Soil gas surveys

Ground-based soil CO_2 and H_2S flux surveys were conducted at Red Crater in February 2014 (233 measurements) and April 2024 (70 measurements), simultaneous ground temperature measurements were made with a soil thermometer (~13 cm deep, lithology permitting). Measurements were made at irregular spacings using the accumulation chamber method (Chiodini et al., 1998), with a West Systems portable fluxmeter (West Systems, 2019). The MULTI-GAS system houses an infrared analyser for CO_2 and H_2O (LI-COR LI-850) and a WS-TOX-H2S electro-chemical sensor for H_2S. To minimise the impact of rainfall on gas flux (Hinkle, 1991; Chiodini et al., 1998), the surveys were conducted on dry days and after a minimum of three days where there was no precipitation (e.g., Yang et al., 2024).

The following equations are used to calculate the CO_2 (F_{CO_2}) and H_2S (F_{H_2S}) fluxes in $g/m^2/day$ (Chiodini et al., 1998; Williams-Jones et al., 2000; West Systems, 2019; Yang et al., 2024):

$$F_{CO_2} = R_{CO_2} \times (86400 \times P \times V)/(10^6 \times R \times T \times A) \times M_{CO_2} \quad (4)$$

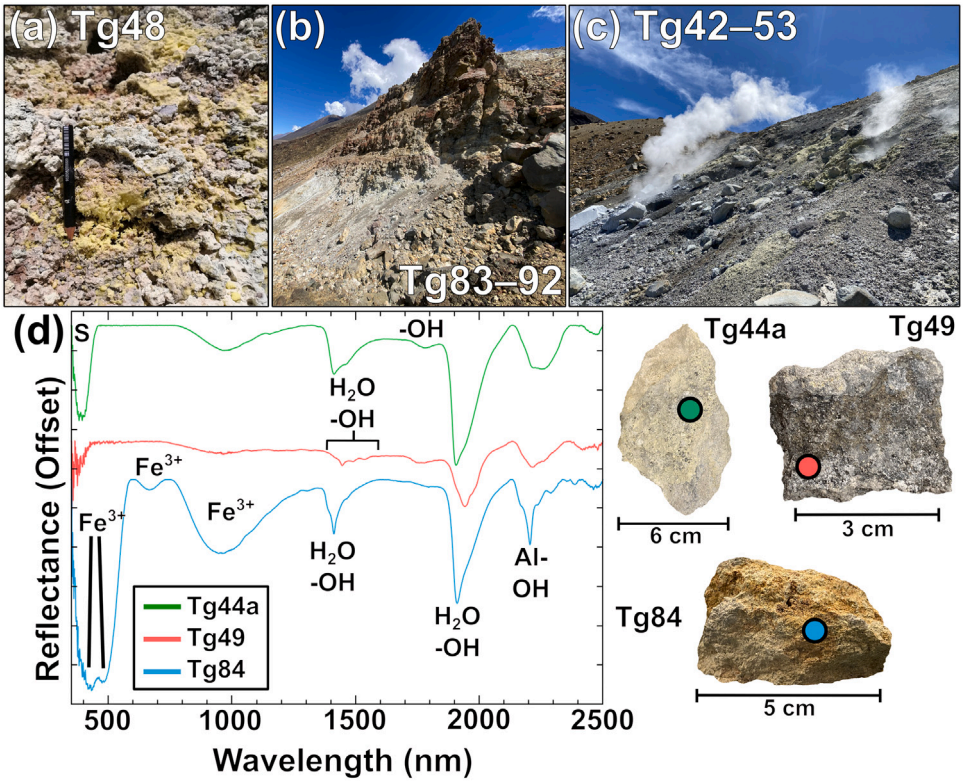

Fig. 2. Field photos of Oturere; samples collected from each area are listed. (a) Typical native sulphur and silica upon tephra deposits, (b) fractured Waitakatorua lava exposed beneath the Oturere geothermal area, (c) native sulphur deposits and silicic alteration at Oturere, and (d) continuum removed reflectance spectra (offset for clarity) highlighting absorption features typical of sulphur (Tg44a), silica (Tg44a), goethite (Tg84), smectite (Tg84), and gypsum (Tg49) minerals from the Emerald Lakes and Oturere, with corresponding samples on the right, dots indicate probe location. See Table 4 for a summary of typical mineral absorption features.

$$F_{H_2S} = R_{H_2S} \times (86400 \times P \times V)/(10^6 \times R \times T \times A) \times M_{H_2S} \quad (5)$$

Where R_{CO_2/H_2S} are raw gas fluxes in ppm/s, P is the ambient air pressure (hPa), V is the dead space volume of the system (0.006186 m^3), R is the gas constant (0.08313510 $bar \cdot L \cdot K^{-1} \cdot mol^{-1}$), T is ambient air temperature in K, A is the area of the chamber (0.0317 m^2) and M_{CO_2/H_2S} are the molecular weights of CO_2 (44.01 g/mol) and H_2S (34.082 g/mol).

Soil CO_2 gas flux data were further processed within Windows Geostatistical Software Library (WinGslib) (see Deutsch and Journel, 1997; Cardellini et al., 2003). Sequential guassian simulations (with a nugget effect of 0.5 and a sill of 1) were run to produce 100 different but equiprobable realisations of unsampled locations within the defined area (e.g., Chiodini et al., 2004; Yang et al., 2024). H_2S data were not subjected to sequential Guassian simulations due to their limited spatial footprint.

Multiple gas sources (e.g., biological, hydrothermal, magmatic) may contribute to diffuse CO_2 emissions and therefore generate a multi-modal distribution of flux values (Cardellini et al., 2003). We used graphical statistical analysis to differentiate between CO_2 degassing populations at Red Crater following methods from Sinclair (1974), Chiodini et al. (1998). Two overlapping populations of CO_2 flux values were identified from an inflection point of their curve on a logarithmic probability plot (Fig. 8). The flux data of the different populations were defined, and the proportion, arithmetic mean CO_2 flux, and range (90% confidence interval) was calculated for each population using the Sichel t estimator (Sichel, 1966; David, 1977) (Table 3).

Table 3
Graphical statistical analysis parameters for outgassing at Red Crater. Mean CO_2 flux (g/m^2/d) and the flux range in the 90% confidence interval.

CO_2 flux population	% of datapoints	Mean CO_2 flux (g/m^2/d) (90% confidence interval flux range)
A	58%	21 (14.3–34.5)
B	42%	1103 (850.4–1548.9)

3. Results

3.1. Red crater alteration mineralogy

Non-altered lithologies have a groundmass composed of predominantly euhedral and subhedral plagioclase laths, euhedral and anhedral clinopyroxenes and minor olivine and titanomagnetite microlites (≤80 μm). Plagioclase is the dominant phenocryst (≥100 μm), followed by clinopyroxene and minor olivine and titanomagnetite. The phenocrysts are generally subhedral, they often exhibit intra-crystal fractures, and well formed individuals display tabular, platy and octagonal habits. Clinopyroxenes display occasional compositional zoning with slight (+≤8 mol%) Mg enrichment and reduced Ca (-≤3 mol%) and Fe (-≤7 mol%) towards the crystal rim, and several also contain titanomagnetite and chromium spinel inclusions. Minor titanomagnetite and olivine phenocrysts are also present in some samples (Tg42a, 44a, 57b), they are mainly subhedral with bladed titanomagnetite and tabular or platy olivine.

Silica polymorphs and native sulphur deposits are widespread across Red Crater. They are the primary alteration minerals at the Emerald Lakes and Oturere (Fig. 6), alongside minor phyllosilicates. Samples from these areas are encrusted with silica and sulphur sublimates, and

Table 4
Summary of alteration minerals at Red Crater, their VNIR-SWIR absorption properties and SEM-EDS observations. See Supplementary Material for full sample list and VNIR-SWIR and SEM-EDS observations.

Minerals	Absorption features (nm)	SEM-EDS observations
Native Sulphur	386, 403	Precipitation within and around void spaces (Tg49).
Amorphous Silica	1408, 1908, 2210	Minor (Tg42a, 45a) to complete (Tg44a, 58) replacement of phenocrysts. Minor (Tg57b) to pervasive (Tg58, 59) silicification of groundmass.
Goethite	433, 487, 674, 966	–
Pyrite	–	Subhedral and euhedral cubic crystals within pores, cracks and the edges of void spaces, and partial infilling of fractures (Tg58).
Kaolin Group	1394, 1413, 2167, 2207	Filling and surrounding void spaces. Occasional botryoidal formations. Otherwise lacking an obvious crystalline shape (Tg58, 59). Occasional replacement of groundmass (Tg58).
Smectite Group	1414, 1464, 1907, 2208	One occurrence of nontronite found within void space (Tg58).
Alunite	1434, 1475, 1764, 2175, 2209	Clusters of medium to fine (≤50 μm) anhedral and pseudocubic crystals, some rims display resorption features, located around the edges of and within void spaces (Tg58, 59). Not found within groundmass or as a phenocryst pseudomorph. Amorphous deposits seen infilling void spaces (Tg57b).
Jarosite	436, 900, 1466, 1852, 2207, 2263	Pseudocubic, ≤10 μm, subhedral (Tg59). Replacing alunite within pore spaces (Tg57b).
Gypsum	1446, 1490, 1539	–
Dolomite	–	10 μm diameter anhedral grain sat within a dissolved rim of plagioclase phenocryst (Tg49).

sit within a heated (up to ~100°C) matrix of cemented tephra (Fig. 2a). VNIR-SWIR reflectance data show absorptions at 386 and 403 nm typical of sulphur (Kokaly et al., 2017), and broad features at 1408, 1908, and 2210 nm, that are indicative of amorphous/poorly crystalline silica (e.g., opal-TC) (Milliken et al., 2008; Simpson and Rae, 2018) (Fig. 2d, Tg44a). Minor occurrences of montmorrillonite and kaolinite on the rims of some of these samples were identified with spectral data, however they were not observed within sample interiors via SEM-EDS analysis. Widespread native sulphur precipitation around void spaces and fractures was identified under SEM-EDS within Tg49 (Fig. 3b), and spectral data confirms its presence within interiors of Tg75a, 83, and 88. Samples maintain a mostly fresh groundmass but exhibit dissolution textures and silicification of plagioclase (Fig. 3a, c), clinopyroxene and olivine phenocrysts. These range from minor (~10–25 μm) surface textures to complete replacement of the crystal. Textures found in feldspars and olivines contain amorphous silica, whereas in clinopyroxenes, they may also expose the underlying groundmass. $\delta^{34}S$ isotope values from Oturere (Tg46, 47, 48) and Northern Emerald Lake crater (Tg54) show minor enrichments in ^{34}S, ranging from 0.9–2.1‰ (Table 5). The presence of silica polymorphs and native sulphur deposits at the Emerald Lakes and Oturere is indicative of a silicic alteration regime, with intense cation leaching via SiO_2 rich, acidic (pH ≤2) hydrothermal fluids, that cool swiftly at the surface, forming local sinters (Stoffregen, 1987; Pirajno, 1992; Corbett and Leach, 1997). Sulphur-rich fluids are expelled at active fumaroles and permeate through surrounding tephra deposits, precipitating elemental crystals (Giggenbach, 1987; Rowe et al., 1992; Rye et al., 1992).

Silica polymorphs, ±kaolinite, ±alunite, ±smectite, ±goethite comprise the second alteration mineral association at Red Crater, which occurs primarily at the North East Crater Wall. Native sulphur deposits are also abundant proximal to fumaroles, and within samples we observe minor jarosite and pyrite. Zones of alteration are typically pink/light brown/orange in colour, consisting of hot (up to ~93°C), cemented matrixes of tephra supporting clasts of fine to coarse scoria and blocks, surrounding lava flows. The majority of samples display SWIR features indicative of a mixture of phyllosilicates, specifically

Table 5
Stable isotope ratios of native sulphur and alunite samples.

Sample	Location	Mineral	$\delta^{34}S_{SO4}$ (± 0.2) ‰	$\delta^{18}O_{SO4}$ (± 0.2) ‰
Tg46	Oturere 39° 08'05.3"S 175° 39'20.5"	Sulphur	2.1	–
Tg47	Oturere 39° 08'05.5"S 175° 39'21.6"E	Sulphur	0.9	–
Tg48	Oturere 39° 08'06.7"S 175° 39'22.7"E	Sulphur	1.3	–
Tg54	Northern Emerald Lake 39° 08'03.2"S 175° 39'20.6"E	Sulphur	0.9	–
Tg57b	North East Crater Wall 39° 08'06.7"S 175° 39'14.7"E	Alunite	2.7	16.03

kaolin (e.g., kaolinite and halloysite) and smectite (e.g., montmorrillonite and nontronite) group minerals (Fig. 4). The two groups can be distinguished by identifying certain absorption features within the VNIR-SWIR spectrum, which are indicative of vibrations of molecular (OH, H_2O) or cation-hydroxyl bonds (e.g., Al-OH, Fe-OH, and Mg-OH) (Bishop et al., 2002, 2008; Simpson and Rae, 2018). Here, kaolin minerals present two doublet absorption features, the first is situated at 1395 and 1415 nm, and the second at 2165 and 2205 nm, with a deeper trough at 2205 nm (Bishop et al., 2008; Santamaría-López et al., 2024), and several secondary features around 2315, 2355, and 2382 nm caused by OH-stretching and lattice vibrations (Ducasse et al., 2020). Smectite group minerals typically have absorption features at 1414, 1464, 1905, and 2204 nm (Simpson and Rae, 2018; Lorenzo et al., 2021). Occasionally, absorption features diagnostic of alunite (1434, 1480, 1764, and a doublet at 2174, 2208 nm) were present alongside phyllosilicates, indicating a mixture of the three minerals at scales of a ≤8 mm. One block proximal to a fumarole (Tg70) displayed absorption features typical of ammonium smectite, with additional features at 2007 and 2112 nm caused by the presence of NH_4 molecules (Felzer et al., 1994) (Fig. 4d, Tg70); these features were not present in any other sample. Goethite is abundant on the crusts of samples, identified

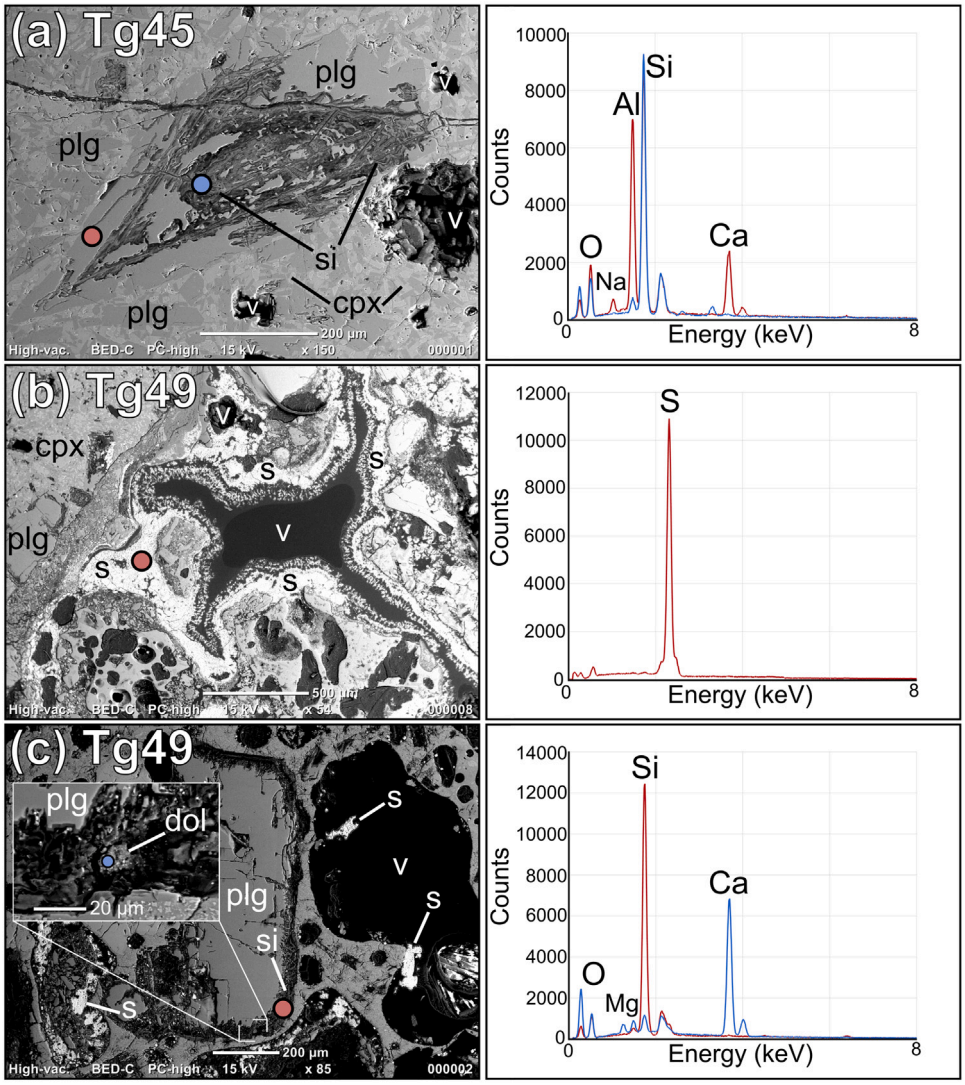

Fig. 3. SEM image (left) and EDS spectra (right) of typical alteration mineralogy from the Emerald Lakes/Oturere. Coloured dots on SEM imagery correspond to points of EDS spectra. Mineral abbreviations; plg, plagioclase; cpx, clinopyroxene; s, sulphur; si, silica; dol, dolomite; v, void space. (a) Silicification of a plagioclase phenocryst surrounded by fresh groundmass, (b) native sulphur precipitation surrounding a pore space of scoria, and (c) dolomite nested within silicified rim of plagioclase phenocryst, minor native sulphur precipitation within void spaces.

by the crystal field transition absorption features at 487 and 674 nm, with a wider feature at 950 nm (Crowley et al., 2003; Kokaly et al., 2017). In hematite, the latter feature is at a shorter wavelength position of 870 nm and thus aids in distinguishing the two minerals (Crowley et al., 2003).

Under SEM, amorphous silica, kaolinite and alunite are the prevalent alteration minerals (Fig. 5b, c). Silica is a common pseudomorph for plagioclase and pyroxene phenocrysts, and is the prevalent replacement mineral for the groundmass. Kaolinite also appears as a replacement of the groundmass but its dominant form is filling and surrounding void spaces, in both cases lacking an obvious crystalline shape (Tg58, 59). Kaolinite are accompanied by clusters of medium to fine (≤50), anhedral to pseudocubic alunite (Fig. 5c) that occasionally exhibit resorption features on their crystal margins. In Tg58, fine, euhedral and subhedral pyrite deposits are found partially filling fractures and pore spaces within the groundmass, but also within intra-crystal fractures (Fig. 5b). Minor jarosite was identified proximal to alunite deposits and as a replacement mineral (Fig. 5a, c); Tg57b provides a clear view of this replacement process within the same network of pore spaces.

Alteration minerals of silica polymorphs, ±kaolinite, ±alunite across samples suggest an advanced argillic environment with acid sulphate alteration at the North East Wall of Red Crater scoria cone (Meyer and Hemley, 1967; Henley and Ellis, 1983; Rye, 2005; John et al., 2008).

Minor alteration phases of gypsum and dolomite minerals were identified within sample Tg49, a piece of scoria with abundant native sulphur deposits and minor silicification, situated on the western edge of Oturere. The gypsum crystals are white/grey, situated in a ~1.5 cm patch in the sample's interior, surrounded by fresh rock, exhibiting a diagnostic triplet absorption feature at 1446, 1490, 1539 nm (Milewski et al., 2019). The isolated deposit of dolomite constitutes an anhedral, 10 µm diameter grain, positioned on the dissolved rim of a plagioclase phenocryst. More dolomite may exist within this sample, confirming this will require a more comprehensive survey under SEM. Interestingly, dolomite has also been observed in samples from Te Maari (Sanchez et al., 2025). Additionally, white mineral deposits were found upon the rims and within pores of scoria (Tg102), sampled from pyroclastic fall deposits adjacent to the Tongariro Alpine Crossing track, on the north-west rim of Red Crater. The area has weak fumarole activity and soil temperatures up to 55.9°C. Spectral data of this white mineral show a triplet absorption feature at 1392, 1407, 1463 nm, and a doublet at 2288 and 2311 nm, adjacent to the 2215 Al-OH feature (Fig. 4d, Tg102). The triplet feature may be a result of a

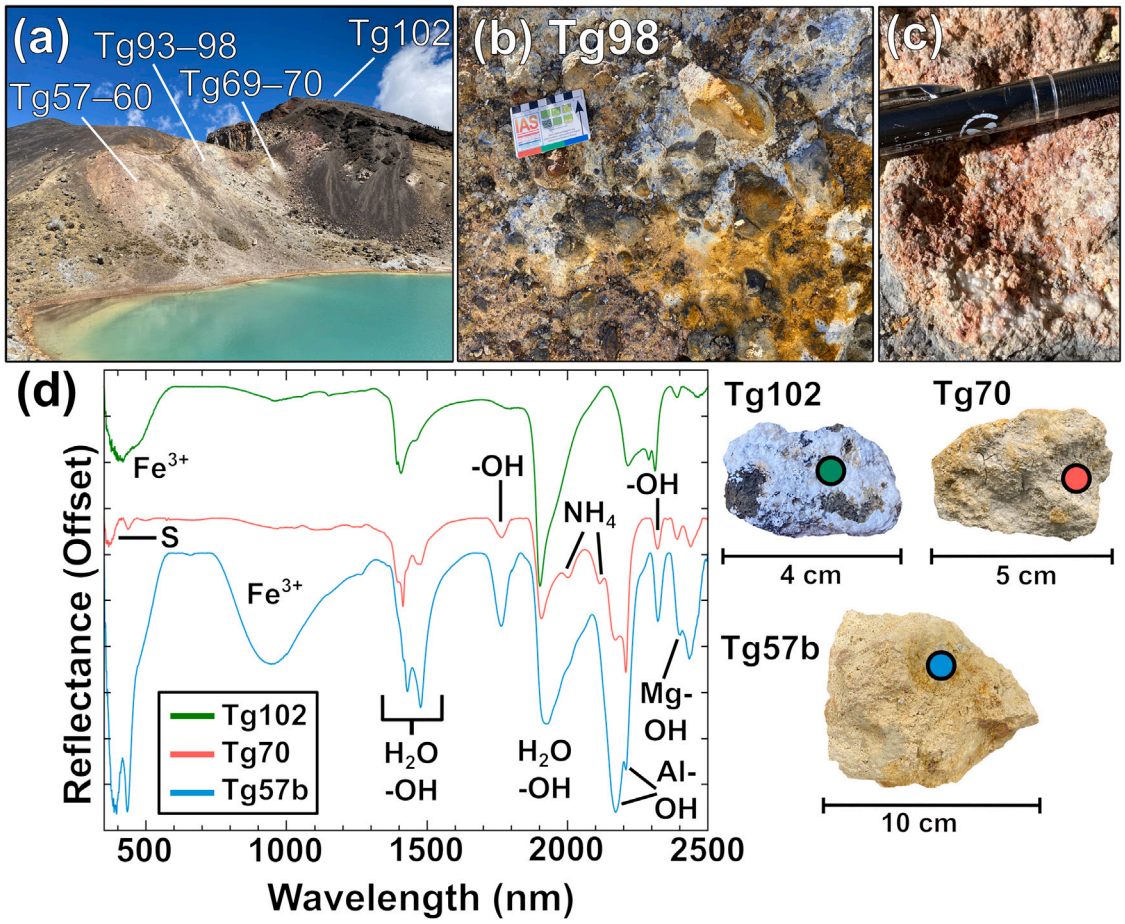

Fig. 4. Field photos of the North East Wall of the Red Crater scoria cone; samples collected from each area are listed. (a) View facing SW of the North East Wall with sample locations labelled, (b) altered scoria bed with kaolinite, alunite, and goethite minerals, (c) crust of opal, goethite and sulphur upon lava, and (d) continuum removed reflectance spectra highlighting typical absorption features of sulphur (Tg70), kaolinite (Tg70), alunite (Tg57b), goethite (Tg57b), and smectite (Tg70, 102), with corresponding samples on the right, dots indicate measurement location. See Table 4 for a summary of typical mineral absorption features.

mixture of kaolinite, montmorrillonite and/or opal minerals. Alternatively, it matches well spectrally with hectorite from the USGS Spectral library (Kokaly et al., 2017). Further sampling, spectroscopy and SEM analysis of this mineral is required for a more accurate confirmation.

3.2. Surface alteration mapping

Supervised image classification of the hyperspectral image using a random forest algorithm was implemented to map alteration units at Red Crater (Fig. 6). The overall accuracy of the classification based on independent validation data is 89% (Eq. (1)). The total area of surface hydrothermal alteration at Red Crater is estimated by the image classification to be 12,968 m^2, 71% of which is silicification (9190 m^2) and 29% is argillic (3778 m^2) (Table 7). Argillic areas were identified by the random forest algorithm due to their unique and diagnostic doublet absorption feature at 2165 and 2205 nm, however spectral noise or steam from geothermal areas (e.g., Oturere) occasionally mimics this feature and leads to the misclassification of these pixels as argillic (Fig. 6). The largest region of argillic alteration is the North East Crater Wall, although discrete areas on and around the rim of the scoria cone were identified, that likely represent hydrothermally altered lithics and lavas of the Rotopaunga andesite described by Bardsley (2004) and Wadsworth et al. (2015). A concentrated area of argillic alteration, identified by absorption features diagnostic of alunite, is also apparent upon Waitakatorua lavas on the east of Oturere Valley. There is no present day geothermal activity in this area, it may therefore be evidence of a fossil hydrothermal system in this area.

The random forest algorithm likely identifies silicification primarily on the basis of its reflection intensity compared to other classes, which is a function of illumination geometry and grain size (Clark and Roush, 1984). The model detected spectral similarities between the silicified lavas at Oturere and the North East Crater Wall, suggesting they share a similar host rock and that the lava at the North East Crater Wall is part of the Taiko Formation. Additionally, spectra of the silicification class contains a relatively shallow and wide absorption feature at 2210 nm which also serves as a feature for its identification (e.g., Rodriguez-Gomez et al., 2021). The region of silicification at the North East Crater Wall may also be partially obscuring argillic areas. Several field samples collected from this area have surface alunite and kaolinite, although this signal was not recognised by the aerial hyperspectral image. The absorption features may have been dampened by the abundance of silica polymorphs within this area compared to argillic minerals, or sensor/atmospheric noise, highlighting the benefits of field sampling as validation for hyperspectral imagery.

The two largest classes mapped were unaltered lava (0.52 km^2) and scoria/tephra (0.24 km^2), and they also accounted for the majority of classification errors (Table 6). Misclassification between the two classes is likely due to multiple factors. First, scoria and tephra deposits

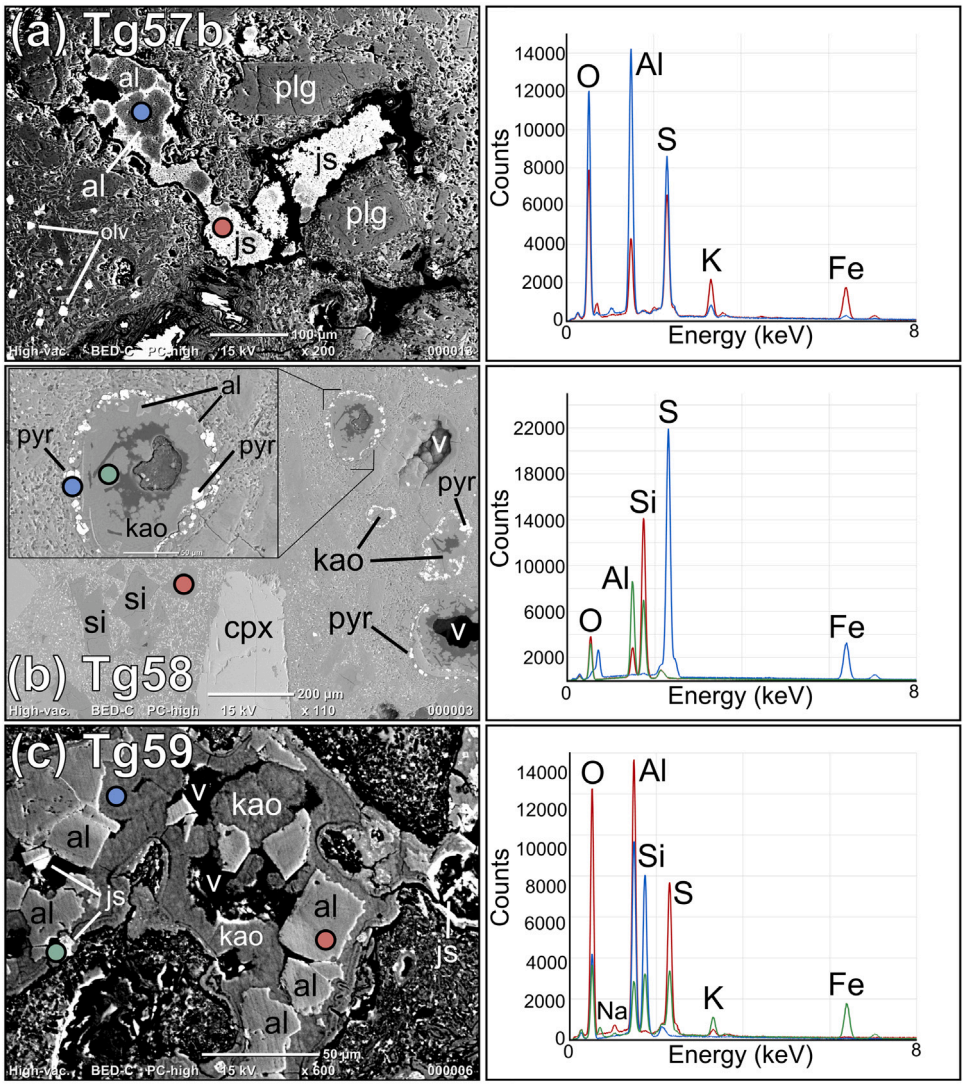

Fig. 5. SEM image (left) and EDS spectra (right) of representative samples from the North East Crater Wall. Coloured dots on SEM imagery correspond to points of EDS spectra. Mineral abbreviations are as follows; plg, plagioclase; cpx, clinopyroxene; olv, olivine; pyr, pyrite; si, silica; kao, kaolinite; al, alunite; js, jarosite; v, void space. (a) Alunite and jarosite infilling the same void space surrounded by an unaltered groundmass with olivine microlites, (b) silica replacing phenocrysts, kaolinite within void spaces accompanied by fine anhedral alunite, pyrite deposits are present within cracks and pores, and (c) region of amorphous kaolinite around and within void spaces, accompanied by subhedral and anhedral, pseudocubic alunite, and minor jarosite, surrounded by a silicified groundmass.

are often found overlying lava flow surfaces (Shane et al., 2017); pixels within the hyperspectral image are 1.2 m in size and therefore training/validation polygons inevitably contain pixels containing the other class (Table 7). Second, both classes exhibit similar reflectance spectra as they are composed of similar primary minerals and show widespread surface oxidation, the latter of which produces distinct Fe^{3+} absorption features around 500 nm. Integrating LiDAR data within the image classification can account for factors such as contrasting surface roughness and may therefore improve the accuracy between the two classes (e.g., Kereszturi et al., 2018).

3.3. Red crater degassing

Four distinct regions of heightened degassing at Red Crater were identified: the North East Crater Wall, Southern Emerald Lake, Oturere, and the northern rim of the scoria cone. These coincide with geothermal surface features and/or hydrothermal alteration (Fig. 7).

Using graphical statistical analysis (Section 2.6), two populations of degassing were identified at Red Crater: population A, characterised by low emissions that may be due to low permeability regions or possibly from biogenic sources (e.g., root/soil respiration (Di Martino et al., 2022)), and population B, high emissions that represent magmatic/hydrothermal processes located around areas of higher permeability (Fig. 8). The mean CO_2 flux of population A is 21 g/m^2/d (14.2–34.5 90% confidence interval) and for population B it is 1103 g/m^2/d (850.4–1548.9).

The mean soil CO_2 emission rate of Red Crater using sequential Gaussian simulations is estimated at 26.2 ±1.5 t/d and raw flux values range from 0.04 to 9320 g/m^2/d. CO_2 emissions of individual geothermal areas at Red Crater were estimated using ordinary kriging in Surfer (Golden Software, 2025). Oturere and the North East Crater Wall dominate emissions with 11.2 and 10.3 t/d respectively (Fig. 7). The highest individual flux value however (9320 g/m^2/d) was measured on the northern rim of the scoria cone, in an area with minor steaming and mineral precipitation, and a soil temperature of 55.9°C.

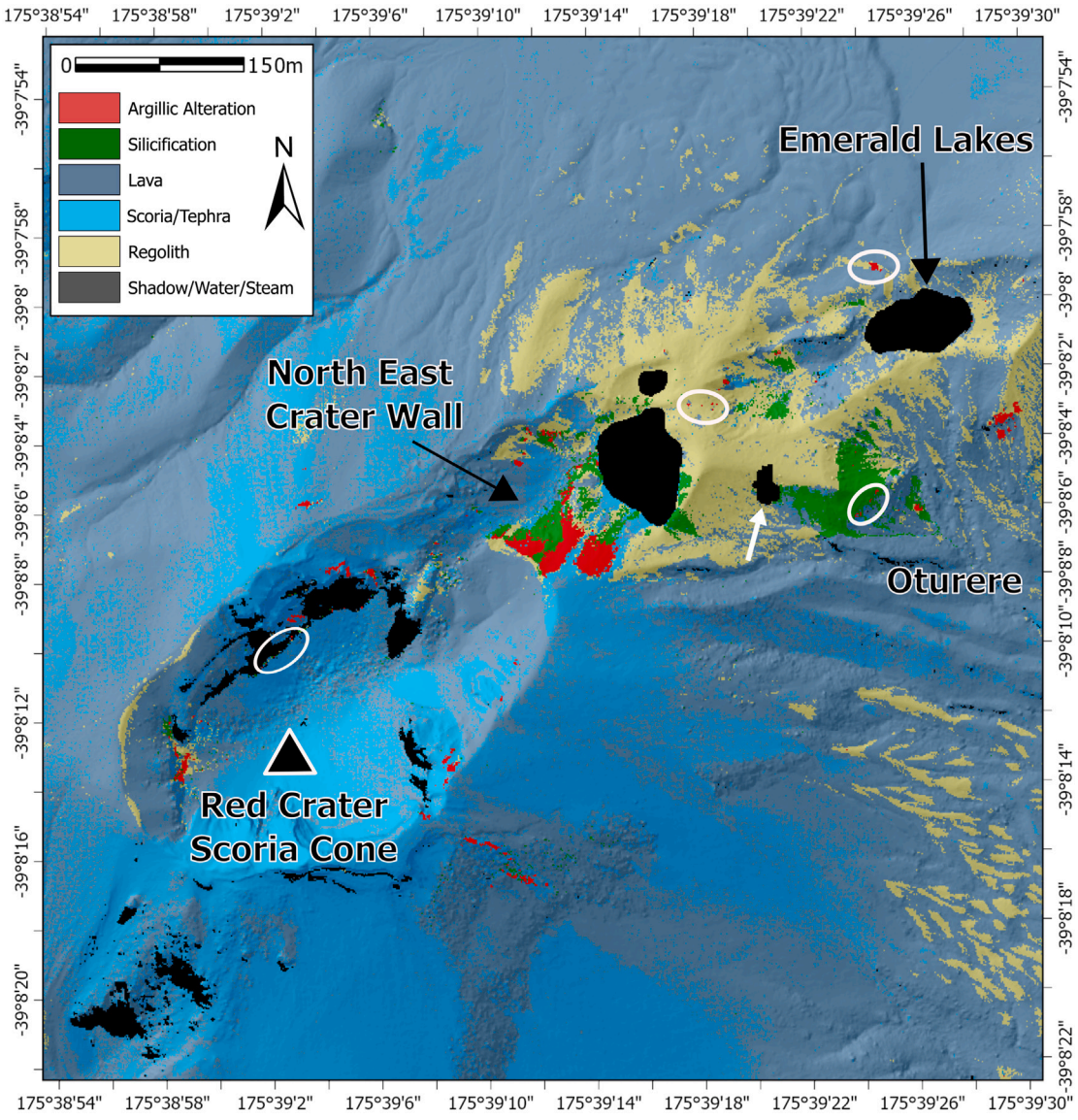

Fig. 6. Red Crater alteration map from the random forest image classification results, draped over a 1 m hillshade. The white ovals highlight several areas misclassified as argillic due to spectral noise. The white arrow indicates steam and shadow from the large fumarole at Oturere. Tongariro 1 m hillshade from Land Information New Zealand.

Table 6
Confusion matrix showing no. of pixels correctly (bold) and incorrectly predicted by the random forest classification (vertical) against the validation population (horizontal).

		Predicted classes						
		Regolith	Scoria/ Tephra	Lava	Argillic Alteration	Silicification	Shadow/ Water/Steam	Total
Reference classes	Regolith	**207**	1	17	0	0	0	225
	Scoria/Tephra	0	**972**	128	0	0	0	1100
	Lava	0	105	**494**	0	0	1	600
	Argillic Alteration	0	0	0	**62**	2	0	64
	Silicification	0	0	1	0	**79**	0	80
	Shadow/Water/Steam	0	1	1	0	0	**198**	200
	Total	207	1079	641	62	81	199	2269

H_2S emissions at Red Crater are confined to areas of hot, steaming ground and active fumaroles. Only 10 of 172 individual H_2S measurements yielded flux values above a threshold of 1 g/m^2/d, ranging from 1.1 to 50.5 g/m^2/d. Oturere and the Southern Emerald Lake have total fluxes of 67.6 and 60.4 g/m^2/d respectively, while the North East Crater Wall emits only 3.1 g/m^2/d.

Through examining CO_2 degassing rates and coinciding soil temperatures three general types of activity can be distinguished (Fig. 9). The first is characterised by high soil temperatures (39–100°C) and high CO_2 fluxes (125–9320 g/m^2/d), indicating permeable areas that overlie high temperature hydrothermal zones. The second type comprises ambient soil temperatures (4–34°C) and heightened degassing (51–2945

Table 7
Class-wise user (Eq. (2)) and producer (Eq. (3)) accuracy based on independent validation data, and their total number of pixels and corresponding area as predicted by the random forest classification.

Class	User's accuracy (%)	Producer's accuracy (%)	Predicted no. of pixels	Predicted total area (m^2)
Regolith	100	92	46,093	66,375
Scoria/Tephra	90	88	166,325	239,509
Lava	77	82	362,906	522,586
Argillic Alteration	100	96	2623	3778
Silicification	97	98	6381	9190
Shadow/Water/Steam	99	99	14,117	20,329

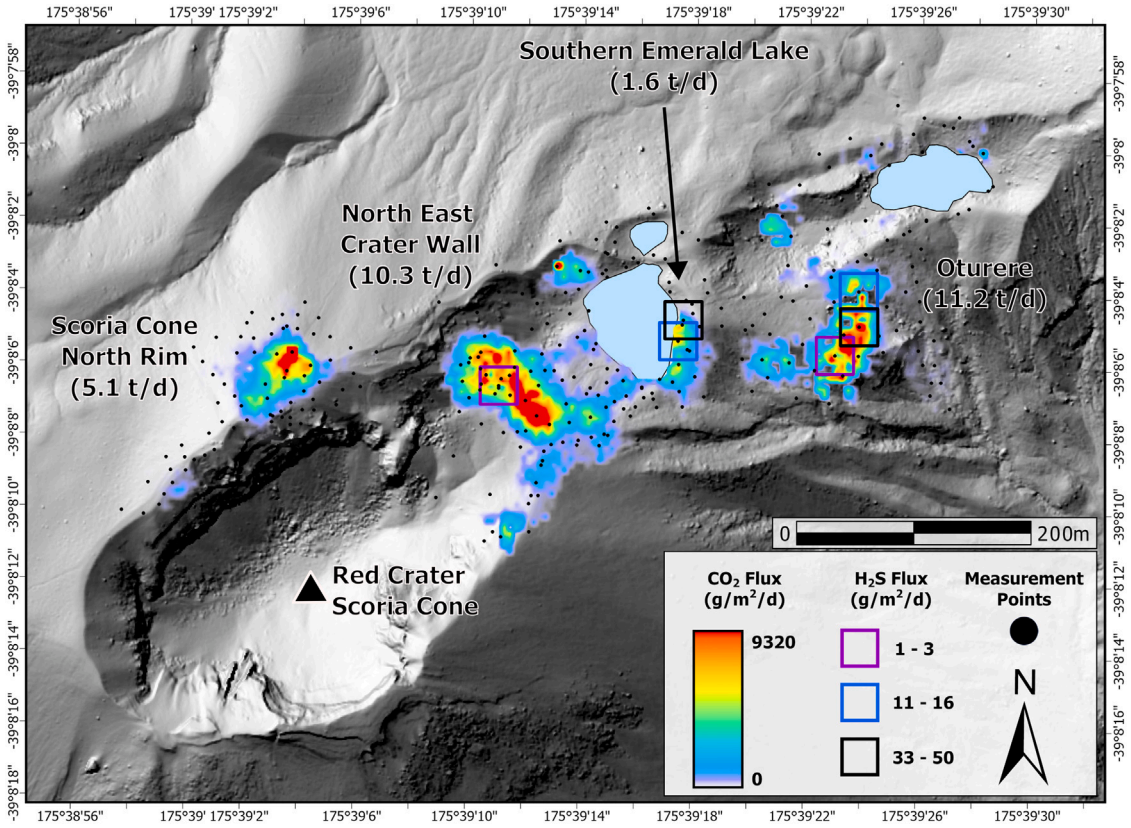

Fig. 7. Map of CO_2 and H_2S fluxes across Red Crater. CO_2 distribution in $g/m^2/d$ from 100 sequential guassian simulations, the average daily emissions from key areas derived via kriging are labelled. H_2S markers are enlarged and grouped for clarity. Tongariro 1 m hillshade from Land Information New Zealand and Emerald Lakes polygons from GNS Science web map service.

$g/m^2/d$). These measurements highlight permeable units that are outside of high temperature hydrothermal areas. The third type consists of areas with ambient soil temperatures and lower degassing rates (≤48 $g/m^2/d$). Typically these are situated outside of hydrothermally altered and geothermal areas. Occasionally they occur in close proximity to areas with high gas fluxes and high soil temperatures, suggesting the fracture or heat pipe feeding that activity is small and concentrated.

4. Discussion

4.1. Hydrothermal alteration at red crater

Hydrothermal alteration at Red Crater represents the surface of an epithermal system with two distinct alteration mineral associations: advanced argillic alteration of the North East Crater Wall of the scoria cone and silicification at the Emerald Lakes and Oturere (Fig. 6). Samples display leaching of Ca, Mg, K and Na cations from the primary mineralogy by acidic fluids, leading to the formation of silica, native sulphur, kaolinite and alunite, typical of acid-sulphate alteration (Henley et al., 1984; Stoffregen, 1987; Klammer, 1997; Barrett and Joseph, 2018).

The textural and geochemical characteristics of alunite can provide insights into the processes and environmental conditions driving acid-sulphate alteration in hydrothermal systems (Seal et al., 2000; Deyell and Dipple, 2005). Alunite may form via several different mechanisms (see Rye, 2005), including magmatic-steam; which involves an ascending SO_2 rich vapour plume that experiences no reduction during disproportionation, and steam-heated; whereby rising H_2S is oxidised at or above the water table, releasing sulphuric acid into the hydrothermal fluid according to the reaction $H_2S + 2O_2 = H_2SO_4$ (Rye et al., 1992). Alunite at Red Crater are rarely well formed, habits are typically anhedral to pseudocubic and medium to fine grained (≤50 μm), which can be indicative of formation within a relatively low temperature environment of ~70–180°C (Deyell et al., 2005). This is in contrast to

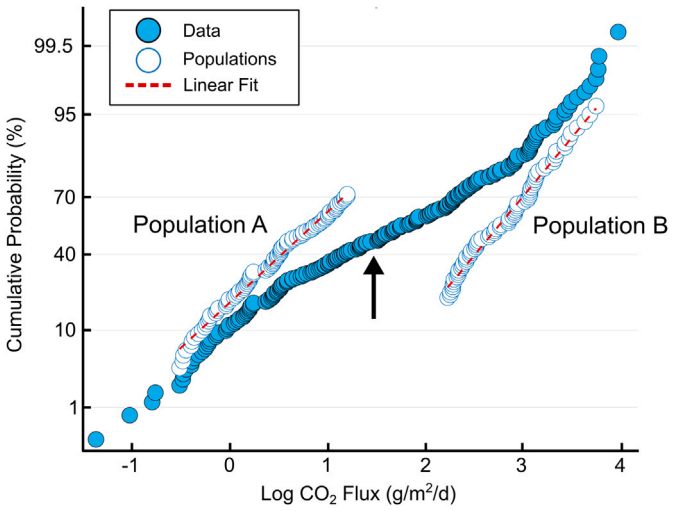

Fig. 8. Cumulative probability plot for Log CO_2 Flux (g/m^2/d), raw data are filled symbols and separate populations are outlines, the black arrow indicates the population inflection point.

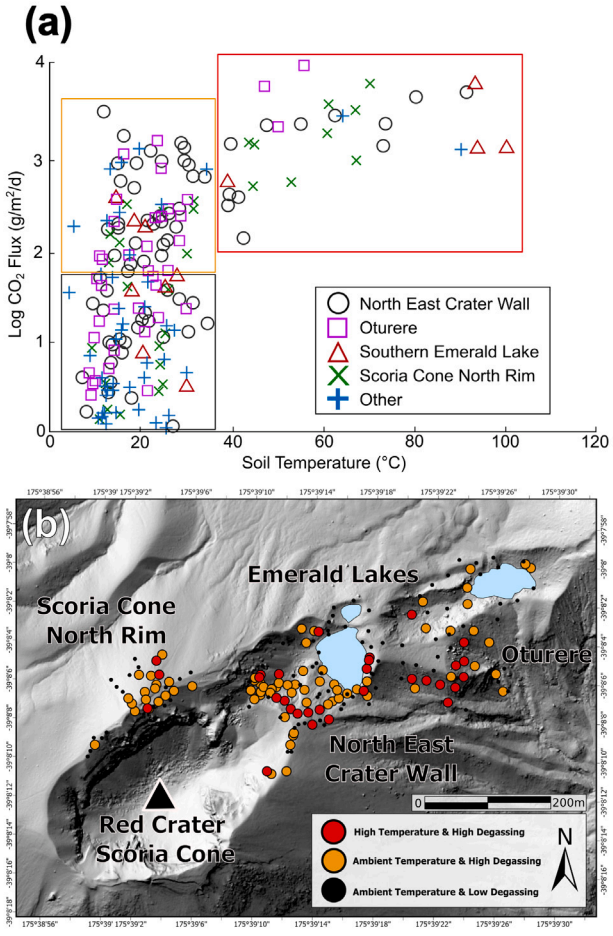

Fig. 9. (a) Log CO_2 flux and soil temperature values grouped by key areas of geothermal activity and alteration at Red Crater, "Other" represents remaining measurements. Red, orange and black boxes denote the split of temperature and degassing types. (b) Map displaying measurement locations coloured by their temperature and degassing class. CO_2 flux values below 1 g/m^2/d are omitted for clarity. Tongariro 1 m hillshade from Land Information New Zealand and Emerald Lakes polygons from GNS Science web map service.

coarser, tabular alunites at the nearby Te Maari (Sanchez et al., 2025) and the neighbouring Mount Ruapehu (Kereszturi et al., 2020), which are typically indications of higher formation temperatures found in magmatic-hydrothermal or magmatic-steam environments (Rye et al., 1992; Deyell and Dipple, 2005). Measured $\delta^{18}O_{SO4}$ and $\delta^{34}S_{SO4}$ isotopic values from alunite sample Tg57b of 2.7‰ and 16.03‰ (Table 5) approximately align (±5‰) with those reported at locations with steam-heated environments (e.g., Tolfa, Italy (Field and Lombardi, 1972) and National dist., NV, USA (Vikre, 1987)) and magmatic-steam environments (e.g., Lake City, CO, USA (Bove et al., 1990) and Alunite Ridge, UT, USA (Cunningham et al., 1984)). The $\delta^{34}S_{SO4}$ value of 2.7‰ for our alunite aligns with recent isotopic data collected from a fumarole at the North East Crater Wall, with $\delta^{34}S_{SO4}$ values of 2.9‰ (2023), 2.3‰ (2024), and 2.8‰ (2025) (GNS Science, 1954). Similar low $\delta^{34}S_{SO4}$ values from fumaroles at Papandayan, Indonesia (Mazot et al., 2008) and Solfatara–Pisciarelli, Italy (Allard et al., 1991, 2015) suggested sulfates are originating from processes dominated by the oxidation of H_2S.

Within the advanced argillic deposits at Red Crater, kaolinite is the dominant phyllosilicate over smectites, which predominantly occur as supergene alteration rinds. Kaolinite is often found with alunite and they both occur as precipitants within fractures and void spaces, rather than mineral pseudomorphs (Fig. 5b, c). Kaolinite forms in relatively low temperature conditions (<150–200°C) (Corbett and Leach, 1997) and can co-exist with alunite under a pH of 3–4 (Stoffregen, 1987). Jarosite is also observed to be replacing alunite (Fig. 5a, c). This process can be characteristic of steam-heated environments and is rare in the magmatic-steam domain (Stoffregen, 1993; Rye and Alpers, 1997; Rye, 2005). The formation of jarosite here may occur due to a lowering of pH and temperature, and/or increase in fO_2 conditions of the system (Stoffregen et al., 2000; Álverez-Valero et al., 2025). Pyrite on the other hand is only observed within pore spaces and fracture networks (Fig. 5b), likely forming as a product of rising H_2S interacting with Fe cations from titanomagnetite, pyroxene, or olivine minerals (Álverez-Valero et al., 2025). Based on textural observations, mineral associations, and isotope values we propose that acid-sulphate alteration at Red Crater is primarily driven by the oxidation of H_2S within a steam-heated environment, with a transitional pH of 2–4 and at temperatures up to ~200°C. This intense acid leaching promotes local silicification of the host rock, and the deposition of opaline silica (Fig. 4c) at the surface from acidic, sulphate and SiO_2 rich fluids (Fournier, 1985; Corbett and Leach, 1997; Rodgers et al., 2002).

Dissolution and resorption features on some alunite crystals (Fig. 5c) indicate that they were partially re-dissolved into the hydrothermal fluid after precipitation, possibly due to changes in the local conditions such as temperature and pH. As a result, the alunite crystals were no longer geochemically stable (Miller et al., 2016). Variations in the local hydrothermal environment may have been caused by changes in host rock permeability and fluid–rock ratios, or from multiple, discrete magmatic intrusion events (e.g., ~1.8 ka (Shane et al., 2017; Pure et al., 2020)), with contrasting degassing regimes. The presence of multiple large lava flows since ~11 ka indicates a relatively long lived and complex plumbing system beneath Red Crater, through which this may have occurred. To further explore this possibility, radiogenic isotopic analysis would be required to accurately constrain alteration ages.

The host rock at Oturere and the Emerald Lakes primarily consists of variably fractured lavas (Fig. 2b), whereas scoriaceous pyroclastic beds characterise the North East Crater Wall (Fig. 4b). The contrasting permeabilities of these units may control fluid flow rates, and therefore fluid–rock interactions (Luhmann et al., 2017; Sanchez et al., 2025), resulting in the distinct alteration associations between the areas (Fig. 10). Fracture networks typically increase permeability and fluid flow rate (Xu and Pruess, 2001; Cox, 2020; Philipp, 2021), thereby reducing fluid–rock interaction and preventing buffering reactions that would increase pH. Silica minerals are stable within these highly acidic

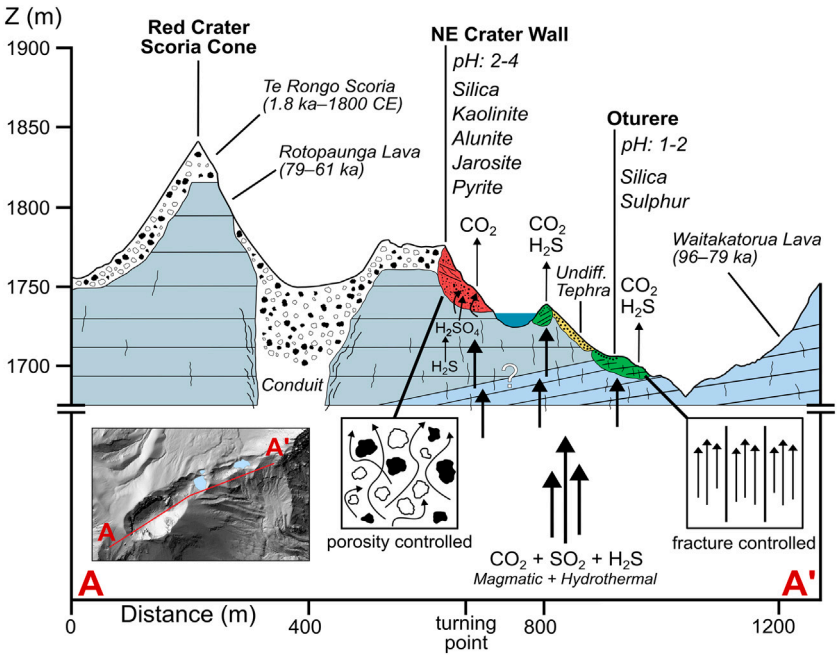

Fig. 10. Conceptual Model for argillic (red) and silicification (green) hydrothermal alteration regimes at Red Crater along the A-A' profile (inset), arrows represent gas and fluid flow through fractures/pathways. Argillic and silicification alteration areas are exaggerated for clarity, their vertical extent is unknown. Unit thicknesses and extents are inferences only and contacts between units are unknown ("?").

environments (pH ≤2) (Stoffregen, 1987) and thus, are the primary alteration minerals present at Oturere and the Emerald Lakes. Conversely, fluid flow at the North East Crater Wall is primarily controlled by the porosity of scoria layers. Scoria typically have relatively low, but highly variable connected porosities (e.g., Mueller et al., 2005; Wright et al., 2009) which will also decrease via compaction or welding (Colombier et al., 2017), thus diffusing rising gas and fluids and reducing flow rate. The filling of fractures and pore spaces by pyrite (Fig. 5b) may further reduce flow rate. Pyrite formation also reflects interactions between H_2S and Fe cations in the host rock (Zimbelman et al., 2005), contributing to the low H_2S emissions in this area. Greater fluid–rock interaction in this setting promotes buffering, thereby raising the pH to ~3–4 where alunite and kaolinite minerals are stable (Stoffregen, 1987).

Following the decline of post-1.8 ka Strombolian activity, a series of hydrothermally driven eruptions excavated sections of the vent, removing a portion of the North East Crater Wall, and forming the Emerald Lakes (Walsh et al., 1998; Bardsley, 2004). These eruptions may have been caused by hydrothermal sealing induced by the deposition of alunite and kaolinite within pore spaces and local silicification of the matrix (Fig. 4), or ground/surface water interactions with the still hot, ponded dyke. Concentrated alteration in this area may have generated localised fracture networks beneath a sealed or altered cap, creating a pathway for volatiles to accumulate and build pressure (e.g., Rowland and Simmons, 2012; Montanaro et al., 2020).

4.2. Degassing and alteration

The spatial footprint of CO_2 degassing highlights several distinct areas with concentrated emissions coinciding with alteration zones (Fig. 7). CO_2 (among H_2S) is one of the key sources of acidity in hydrothermal systems (Giggenbach, 1984) and acts as a mineralising fluid promoting alteration (Giggenbach, 1984; Lowenstern, 2001). Localised heat pipes, fracture networks and/or impermeable subsurface barriers are regulating the degassing and alteration processes at Red Crater (Fig. 9).

H_2S emissions at Red Crater are primarily concentrated at Oturere and the Southern Emerald Lake, with total fluxes of 67.6 and 60.4 g/m^2/d respectively, conversely, emissions at the North East Crater Wall are only 3.1 g/m^2/d. This could be caused by heightened groundwater scrubbing of H_2S at the Crater Wall (e.g., Symonds et al., 2001), or structural (i.e., faults or fractures) and porosity/permeability differences between the two areas controlling flow rates (Fig. 10). Alunite occurs in multiple samples at the North East Crater Wall (Fig. 4 and Fig. 5), but it was not identified at Oturere and the Southern Emerald Lake. Alunite may form through the oxidation of H_2S at or above the water table, producing sulphuric acid that leaches Al, Na and K ions from primary feldspars, pyroxenes, and glass from the surrounding wall rock (Rye et al., 1992; Hedenquist and Arribas, 2022). A significant portion of the rising H_2S at the North East Crater Wall is likely converted to sulphuric acid at shallow depths, forming alunite and removing H_2S from the vapour phase, thereby reducing surface emissions. Rising H_2S may also be consumed via reactions with Fe cations from primary minerals (e.g., pyroxene, olivine) to form pyrite (Álverez-Valero et al., 2025) (Fig. 5b). The absence of alunite and pyrite, coupled with higher H_2S emissions at Oturere and the Southern Emerald Lake, suggests that most of the H_2S escapes to the surface rather than oxidising or reacting with the surrounding rock. This is likely due to the higher porosity/permeability of the host rock at Oturere (i.e., the fractured Waitakatorua lava flow; Fig. 2b) and the Southern Emerald Lake compared to the North East Crater Wall, which reduces residence time and limits oxidation.

4.3. Hydrothermal alteration on multi-vent composite volcanoes

Tongariro hosts a hydrothermal system extending from Ngāuruhoe's northern flank to Upper Te Maari (Walsh et al., 1998; Miller and Williams-Jones, 2016; Sanchez et al., 2025) and hydrothermal alteration deposits are only observed proximal to eruptive vents and Ketetahi springs. Previously active vents such as Blue Lake and the South Crater area display no surface geothermal activity, yet their surface alteration deposits are evidence of fossil hydrothermal systems they once hosted. Surface alteration deposits are present on the crater wall and ridge surrounding the vent occupying Blue Lake (Simons, 2014; Miller and Williams-Jones, 2016). Similarly, alteration deposits including alunite, cristobalite and smectites are present on the walls

and ridgeline of South Crater, forming part of the summit of Mount Tongariro (1967 m) (Lecointre et al., 2002; Cole et al., 2018). Argillic alteration of the Waitakatorua Member deposits was identified within this study via laboratory and airborne hyperspectral imaging (Fig. 6). These lavas form a ridge from Oturere and Mangahouhounui Valley and were erupted from a vent proximal to Central Crater ~96–79 ka (Pure et al., 2020). The alteration here may be evidence of a short-lived fossil hydrothermal system in this area, or these are just discrete areas of heightened fluid flow within permeable units (e.g., auto-brecciated horizons, pyroclastic layers). Currently active vents (Red Crater, Ngāuruhoe, Te Maari, Ketetahi) host hydrothermal surface manifestations that coincide with areas of alteration, which are focused around areas of heightened CO_2 and H_2S degassing (Fig. 7). These vent-focused areas demonstrate that hydrothermal alteration on Tongariro is driven primarily by repeated magmatic intrusions, sourced from an underlying mush at ~4 and 12.5 km depth below sea level (Heise et al., 2024). Subsequently, degassed volatiles (e.g., CO_2, H_2S, SO_2) interact with vapour and condensate within the overall hydrothermal system to produce acidic hydrothermal fluids (Rye et al., 1992; Symonds et al., 2001). The most recent example of this in action was the magmatic intrusion leading to the two eruptions of Te Maari in 2012. Subsequent degassing of the dyke lead to an increase in gas emissions (Christenson et al., 2013), including a heightened H_2S flux of 350 t/d (Jolly et al., 2014). This magmatically-driven increase in activity and acidity of Te Maari's hydrothermal system would have created conditions conducive to an increase in hydrothermal alteration of the surrounding rock. This creates localised and relatively short-lived hydrothermal "systems" confined to individual vents and bounded by faults, which explain the lack of connectivity between individual surface features across the volcano (Miller et al., 2018).

Over longer timescales, these repeated sequences of degassing induced hydrothermal alteration may weaken the host rock via intense cation leaching to such a degree that permeability and porosity are increased (e.g., Mayer et al., 2016), developing a feedback loop in which the alteration further induces degassing, further promoting alteration and so on. This is dependant on the mineralogy and dynamics of alteration. For example, clay precipitation within pore spaces can reduce permeability (Heap et al., 2019), while silicification can simultaneously decrease matrix porosity and permeability (Berger and Henley, 2011) but can be conducive to the development of permeable fracture networks (Heap et al., 2020). Whether the longevity of volcanic activity and alteration at individual vents of Tongariro could have developed to such a stage has not been studied, however it may be occurring at the neighbouring Mount Ruapehu which has a long-lived, nested hydrothermal system that has been active over its 200 ka history (Kereszturi et al., 2020).

4.4. Implications for volcanic hazards

The North East Crater Wall hosts argillic alteration units including clay precipitation within and around pore spaces and silicification of the groundmass, whereas alteration units at Oturere involve silicification and the deposition of native sulphur sublimates. Argillic alteration in particular has been identified as key to inducing volcanic flank collapse at composite volcanoes (e.g., Mount Rainier, USA (Reid et al., 2001)). The presence of clays within these alteration units reduces rock strength (Potro and Hürlimann, 2009; Heap et al., 2021) and can promote ductile deformation when placed under stress, leading to pore collapse (Mordensky et al., 2019). The silicification of host rocks increases their strength characteristics (Callahan et al., 2019), and can initially diminish the matrix permeability and porosity (Dobson et al., 2002), yet due to a propensity for brittle failure behaviour, silicification also favours the formation of permeability-enhancing fractures (Berger and Henley, 2011; Heap et al., 2020). Current-day topography around Red Crater is relatively low relief and most of the alteration areas are mapped on a topographic saddle between the Red Crater scoria cone and a ridge formed by the Waitakatorua Member that spans the Oturere and Mangahouhounui valleys; this seems an unlikely source for future mass flows. However, future studies should be employing limit equilibrium methods to quantify flank stability more accurately using factor of safety (e.g., Vicente et al., 2025). Additionally, geophysical data (e.g., gravity (Miller and Williams-Jones, 2016) and magnetic (Kereszturi et al., 2020)) can provide a depth component and total volume estimates to alteration maps, which are key for detailed slope instability studies.

Clay, native sulphur, sulphide and sulphate deposition within pores and fractures may also cause a decrease in the overall permeability of the rock units. This may restrict gas and fluid flow, therefore increasing the potential for hydrothermal sealing and over-pressurisation within the system and a subsequent phreatic eruption (Kilgour et al., 2010; Farquharson et al., 2017; Mayer et al., 2017; Heap et al., 2019; Mick et al., 2021). The aforementioned processes contributed to the flank collapse and subsequent eruption at Tongariro's Te Maari in 2012 (Vicente et al., 2025), and were likely the primary causes of phreatic eruptions at Whakaari in 2016 and 2019 (Kilgour et al., 2021). The present CO_2 flux at Red Crater (Fig. 7) indicates that fluid pathways are unsealed; the system is currently "open" and overpressure is unlikely. However, continued hydrothermal alteration can modify the strength, porosity, and permeability of these areas; and this state may therefore be subject to change.

Considering Red Crater's numerous (Moebis et al., 2011) and relatively recent (Scott and Potter, 2014) activity in historic times, and the present mineral associations, the potential for future hydrothermally induced activity should be incorporated as part of a robust hazard assessment for this vent.

5. Conclusions

Through a combination of field, laboratory and remote sensing techniques, we identifed and mapped two distinct styles of hydrothermal alteration at Red Crater. Advanced argillic alteration of the North East Crater Wall, that transitions into silicification towards the Emerald Lakes and Oturere. Advanced argillic units were also identified on Waitakatorua eruptives to the east of Oturere, and may be evidence of a relict hydrothermal system. Argillic facies are characterised by silicification, ±kaolinite, ±alunite. This mineral paragenesis, in combination with textural analysis and isotope data, indicates a steam-heated acid-sulphate formation environment, with a transitional pH of 2–4, at temperatures up to ~200°C.

Oturere and the Emerald Lakes are characterised by silicification with native sulphur sublimates, and geothermal manifestations of the underlying hydrothermal system (hot springs, hot steaming ground, fumaroles). Acid leaching of Mg, Fe, K and Ca cations at pH ≤2 causes local silicification of the host rock, and local sinters of amorphous silica are formed via the rapid cooling of SiO_2 rich hydrothermal fluids. The differing mineral associations between these areas of silicification and the North East Crater Wall suggest contrasting porosity and permeability characteristics of their immediate host rock, which exert control over fluid migration rates, and therefore regulate fluid–rock interaction and alteration processes.

Hydrothermal alteration deposits at Tongariro are confined to currently (e.g., Red Crater, Te Maari, Ngāuruhoe, Ketetahi) and previously (e.g., Blue Lake, South Crater, Central Crater) active vents. Repeated magmatic intrusions and ensuing degassing that fuel eruptive activity at these vents lead to the creation of multiple, concurrently active, localised, and relatively short-lived hydrothermal "systems" that evolve at individual vents throughout their lifespan.

Future work should incorporate rock mechanics data of the present minerals and subsurface geophysical mapping to constrain lithological strength under varying pore pressurisations and the extent of hydrothermal alteration at depth. These data, integrated with our high resolution surface mapping, can be used to constrain areas prone to hydrothermally induced hazards at this active vent.

CRediT authorship contribution statement

Daniel Sturgess: Writing – review & editing, Writing – original draft, Software, Methodology, Investigation, Formal analysis, Data curation, Conceptualization. **Gabor Kereszturi:** Writing – review & editing, Supervision, Software, Resources, Methodology, Investigation, Funding acquisition, Conceptualization. **Agnes Mazot:** Writing – review & editing, Supervision, Resources, Investigation, Formal analysis, Data curation. **Rachelle Sanchez:** Writing – review & editing, Investigation. **Antonio M. Álvarez-Valero:** Writing – review & editing, Resources, Investigation, Funding acquisition. **Vladyslav Zakharovskyi:** Writing – review & editing, Software, Formal analysis, Data curation.

Declaration of competing interest

The authors declare that they have no known competing financial interests or personal relationships that could have appeared to influence the work reported in this paper.

Acknowledgements

This study was supported by the Rutherford Discovery Fellowship (“Caught in action - volcano surveillance with hyperspectral remote sensing”; RDF-MAU2003). Álvarez-Valero is supported by Spanish project EruptING (PID2021-127189OB-I00 MCIN/AEI/10.13039/501100011033/FEDER, UE). The authors are very grateful to Iwi within Tongariro National Park and New Zealand’s Department of Conservation for granting permission for sampling work (63618-GEO). We thank Geoffrey Robert and Janine Krippner for field assistance; Anja Moebis, Maia Kidd, and Geoff Kilgour for supporting lab work; Ery Hughes for assisting with GeoNet data; Ruby Stevens for GIS support; and HySpex, Land Pro, and Applanix for help acquiring and processing aerial hyperspectral survey data. We thank Michael Heap and two anonymous reviewers for their valuable comments that improved the manuscript. The New Zealand Basemap and 1 m DEM used in this paper are in the public domain, accessed from Land Information New Zealand’s website (https://data.linz.govt.nz/). Geological units and Emerald Lakes polygons are GIS layers from the GNS Science web map service (https://gis.gns.cri.nz/server/rest/services).

Data availability

The supplementary file provided includes sample information, spectral library, and soil gas survey data. GNS Science (1954) https://doi.org/10.21420/PSP7-KW60 data available on request from GeoNet.

Appendix A. Supplementary data

Supplementary material related to this article can be found online at https://doi.org/10.1016/j.jvolgeores.2026.108535.

References

Aizawa, K., Ogawa, Y., Ishido, T., 2009. Groundwater flow and hydrothermal systems within volcanic edifices: Delineation by electric self-potential and magnetotellurics. J. Geophys. Res.: Solid Earth (ISSN: 21699356) 114 (1), http://dx.doi.org/10.1029/2008JB005910.

Allard, P., Maiorani, A., Tedesco, D., Cortecci, G., Turi, B., 1991. Isotopic study of the origin of sulfur and carbon in Solfatara fumaroles, Campi Flegrei caldera. J. Volcanol. Geotherm. Res. (ISSN: 03770273) 48 (1–2), 139–159. http://dx.doi.org/10.1016/0377-0273(91)90039-3, URL https://linkinghub.elsevier.com/retrieve/pii/0377027391900393.

Allard, P., Maiorani, A., Tedesco, D., Cortecci, G., Turi, B., 2015. Native sulfur, sulfates and sulfides from the active Campi Flegrei volcano (southern Italy): Genetic environments and degassing dynamics revealed by mineralogy and isotope geochemistry. J. Volcanol. Geotherm. Res. (ISSN: 03770273) 304, 180–193. http://dx.doi.org/10.1016/j.jvolgeores.2015.08.017.

Álverez-Valero, A., Kereszturi, G., Sanchez, R., Benavente, D., Pérez-Coca, C., Suárez, M., Christenson, B., Imura, T., Ban, M., 2025. Alteration minerals and their formation environments in intrusion related hydrothermal systems at Ruapehu (New Zealand) – New insights from mass balance and thermodynamic modelling. http://dx.doi.org/10.2139/ssrn.5915238, Available at SSRN: URL https://www.ssrn.com/abstract=5915238.

Ault, W.V., Jensen, M.L., 1963. Summary of sulfur isotope standards. In: Biogeochemistry of Sulfur Isotopes, National Science Foundation Symposium Proceedings. New Haven, pp. 506–567.

Ball, J.L., Taron, J., Reid, M.E., Hurwitz, S., Finn, C., Bedrosian, P., 2018. Combining multiphase groundwater flow and slope stability models to assess stratovolcano flank collapse in the cascade range. J. Geophys. Res.: Solid Earth (ISSN: 21699356) 123 (4), 2787–2805. http://dx.doi.org/10.1002/2017JB015156.

Bardsley, C., 2004. Physical volcanology of Red Crater, Tongariro (Ph.D. thesis). University of Waikato, Hamilton.

Barrett, T.J., Joseph, E.P., 2018. Extreme alteration in an acid-sulphate geothermal field: Sulphur Springs, Saint Lucia. Chem. Geol. (ISSN: 00092541) 500, 103–135. http://dx.doi.org/10.1016/j.chemgeo.2018.09.028.

Berger, B.R., Henley, R.W., 2011. Magmatic-vapor expansion and the formation of high-sulfidation gold deposits: Structural controls on hydrothermal alteration and ore mineralization. Ore Geol. Rev. (ISSN: 01691368) 39 (1–2), 75–90. http://dx.doi.org/10.1016/j.oregeorev.2010.11.004.

Bishop, J.L., Lane, M.D., Dyar, M.D., Brown, A.J., 2008. Reflectance and emission spectroscopy study of four groups of phyllosilicates: smectites, kaolinite-serpentines, chlorites and micas. Clay Miner. (ISSN: 0009-8558) 43 (1), 35–54. http://dx.doi.org/10.1180/claymin.2008.043.1.03.

Bishop, J., Murad, E., Dyar, M.D., 2002. The influence of octahedral and tetrahedral cation substitution on the structure of smectites and serpentines as observed through infrared spectroscopy. Clay Miner. (ISSN: 0009-8558) 37 (4), 617–628. http://dx.doi.org/10.1180/0009855023740064.

Bove, D., Rye, R., Hon, K., 1990. Evolution of the Red Mountain alunite deposit, Lake City, Colorado. Tech. Rep., http://dx.doi.org/10.3133/ofr90235, URL https://pubs.usgs.gov/publication/ofr90235.

Breiman, L., 2001. Random forests. Mach. Learn. 45, 5–32. http://dx.doi.org/10.1023/A:1010933404324.

Browne, P.R.L., 1978. Hydrothermal alteration in active geothermal fields. Annu. Rev. Earth Planet. Sci. (ISSN: 0084-6597) 6 (1), 229–248. http://dx.doi.org/10.1146/annurev.ea.06.050178.001305, URL https://www.annualreviews.org/doi/10.1146/annurev.ea.06.050178.001305.

Callahan, O.A., Eichhubl, P., Olson, J.E., Davatzes, N.C., 2019. Fracture mechanical properties of damaged and hydrothermally altered rocks, Dixie Valley-Stillwater Fault Zone, Nevada, USA. J. Geophys. Res.: Solid Earth (ISSN: 21699356) 124 (4), 4069–4090. http://dx.doi.org/10.1029/2018JB016708.

Cardellini, C., Chiodini, G., Frondini, F., 2003. Application of stochastic simulation to CO2 flux from soil: Mapping and quantification of gas release. J. Geophys. Res.: Solid Earth (ISSN: 21699356) 108 (B9), http://dx.doi.org/10.1029/2002jb002165.

Chiodini, G., Avino, R., Brombach, T., Caliro, S., Cardellini, C., De Vita, S., Frondini, F., Granirei, D., Marotta, E., Ventura, G., 2004. Fumarolic and diffuse soil degassing west of Mount Epomeo, Ischia, Italy. J. Volcanol. Geotherm. Res. (ISSN: 03770273) 133 (1–4), 291–309. http://dx.doi.org/10.1016/S0377-0273(03)00403-7.

Chiodini, G., Cioni, R., Guidi, M., Raco, B., Marini, L., 1998. Soil CO2 flux measurements in volcanic and geothermal areas. Appl. Geochem. (ISSN: 08832927) 13 (5), 543–552. http://dx.doi.org/10.1016/S0883-2927(97)00076-0, URL https://linkinghub.elsevier.com/retrieve/pii/S0883292797000760.

Christenson, B., Britten, K., Mazot, A., Fitzgerald, J., 2013. The 2012 Eruption of Te Mari, New Zealand: Characteristics of a shallow magmatic degassing event. In: AGU Fall Meeting Abstracts.

Clark, R.N., 1999. Spectroscopy of rocks and minerals, and principles of spectroscopy. In: Rencz, A.N. (Ed.), Remote Sensing for the Earth Sciences. John Wiley & Sons, Chichesterm UK, pp. 3–58, URL http://speclab.cr.usgs.govhttp://speclab.cr.usgs.gov/PAPERS.refl-mrs/.

Clark, R.N., King, T.V., Klejwa, M., Swayze, G.A., Vergo, N., 1990. High spectral resolution reflectance spectroscopy of minerals. J. Geophys. Res. (ISSN: 01480227) 95 (B8), http://dx.doi.org/10.1029/jb095ib08p12653.

Clark, R.N., Roush, T.L., 1984. Reflectance spectroscopy: quantitative analysis techniques for remote sensing applications. J. Geophys. Res. (ISSN: 01480227) 89 (B7), 6329–6340. http://dx.doi.org/10.1029/JB089iB07p06329.

Cole, R.P., White, J.D., Conway, C.E., Leonard, G.S., Townsend, D.B., Pure, L.R., 2018. The glaciovolcanic evolution of an andesitic edifice, South Crater, Tongariro volcano, New Zealand. J. Volcanol. Geotherm. Res. (ISSN: 03770273) 352, 55–77. http://dx.doi.org/10.1016/j.jvolgeores.2017.12.003.

Colombier, M., Wadsworth, F.B., Gurioli, L., Scheu, B., Kueppers, U., Di Muro, A., Dingwell, D.B., 2017. The evolution of pore connectivity in volcanic rocks. Earth Planet. Sci. Lett. (ISSN: 0012821X) 462, 99–109. http://dx.doi.org/10.1016/j.epsl.2017.01.011.

Congalton, R.G., 1991. A review of assessing the accuracy of classifications of remotely sensed data. Remote Sens. Environ. (ISSN: 00344257) 37 (1), 35–46. http://dx.doi.org/10.1016/0034-4257(91)90048-B, URL https://linkinghub.elsevier.com/retrieve/pii/003442579190048B.

Corbett, G.J., Leach, T.M., 1997. Southwest Pacific Rim Gold-Copper Systems: Structure, Alteration, and Mineralization. Tech. Rep.

Corrado, F., Putzolu, F., Armstrong, R.N., Mondillo, N., Chirico, R., Casarotto, B., Massironi, M., Fuller, D., Ball, R., Herrington, R.J., 2025. Application of satellite and proximal hyperspectral sensing to target lithium mineralization in volcano-sedimentary deposits: A case study from the McDermitt caldera, USA. Remote Sens. Environ. (ISSN: 00344257) 323, http://dx.doi.org/10.1016/j.rse.2025.114724.

Cox, S.F., 2020. Chapter 2: The dynamics of permeability enhancement and fluid flow in overpressured, fracture-controlled hydrothermal systems. In: Applied Structural Geology of Ore-Forming Hydrothermal Systems. Society of Economic Geologists, pp. 25–82. http://dx.doi.org/10.5382/rev.21.02.

Craig, H., 1961. Standard for reporting concentrations of deuterium and oxygen-18 in natural waters. Science (ISSN: 0036-8075) 133 (3467), 1833–1834. http://dx.doi.org/10.1126/science.133.3467.1833, URL https://www.science.org/doi/10.1126/science.133.3467.1833.

Crósta, A.P., Sabine, C., Taranik, J.V., 1998. Hydrothermal alteration mapping at Bodie, California, using AVIRIS hyperspectral data. Remote Sens. Environ. (ISSN: 00344257) 65 (3), 309–319. http://dx.doi.org/10.1016/S0034-4257(98)00040-6, URL https://linkinghub.elsevier.com/retrieve/pii/S0034425798000406.

Crowley, J.K., Williams, D.E., Hammarstrom, J.M., Piatak, N., Chou, I.M., Mars, J.C., 2003. Spectral reflectance properties (0.4-2.5 μm) of secondary Fe-oxide, Fe-hydroxide, and Fe-sulphate-hydrate minerals associated with sulphide-bearing mine wastes. Geochem.: Explor. Environ. Anal. (ISSN: 14677873) 3 (3), 219–228. http://dx.doi.org/10.1144/1467-7873/03-001.

Crucil, G., Castaldi, F., Aldana-Jague, E., van Wesemael, B., Macdonald, A., Oost, K., 2019. Assessing the performance of UAS-Compatible multispectral and hyperspectral sensors for soil organic carbon prediction. Sustain. (Switzerland) (ISSN: 20711050) 11 (7), http://dx.doi.org/10.3390/su11071889.

Cunningham, C.G., Rye, R.O., Steven, T.A., Mehnert, H.H., 1984. Origins and exploration significance of replacement and vein-type alunite deposits in the Marysvale volcanic field, West Central Utah. Econ. Geol. (ISSN: 0361-0128) 79 (1), 50–71. http://dx.doi.org/10.2113/gsecongeo.79.1.50.

David, M., 1977. Geostatistical Ore Reserve Estimation. Elsevier Scientific Publishing Company, New York.

Dempsey, D.E., Cronin, S.J., Mei, S., Kempa-Liehr, A.W., 2020. Automatic precursor recognition and real-time forecasting of sudden explosive volcanic eruptions at Whakaari, New Zealand. Nat. Commun. (ISSN: 20411723) 11 (1), http://dx.doi.org/10.1038/s41467-020-17375-2.

Deutsch, C.V., Journel, A.G., 1997. GSLIB: Geostatistical Software Library and User's Guide Second Edition. Oxford University Press.

Deyell, C.L., Dipple, G.M., 2005. Equilibrium mineral-fluid calculations and their application to the solid solution between alunite and natroalunite in the El Indio-Pascua belt of Chile and Argentina. Chem. Geol. (ISSN: 00092541) 215 (1-4 SPEC. ISS.), 219–234. http://dx.doi.org/10.1016/j.chemgeo.2004.06.039.

Deyell, C.L., Rye, R.O., Landis, G.P., Bissig, T., 2005. Alunite and the role of magmatic fluids in the Tambo high-sulfidation deposit, El Indio-Pascua belt, Chile. Chem. Geol. (ISSN: 00092541) 215 (1-4 SPEC. ISS.), 185–218. http://dx.doi.org/10.1016/j.chemgeo.2004.06.038.

Di Martino, R.M., Gurrieri, S., Camarda, M., Capasso, G., Prano, V., 2022. Hazardous changes in soil CO2 emissions at Vulcano, Italy, in 2021. J. Geophys. Res.: Solid Earth (ISSN: 21699356) 127 (11), http://dx.doi.org/10.1029/2022JB024516.

Dobson, P.F., Kneafsey, T.J., Hulen, J., Simmons, A., 2002. Porosity, permeability and fluid flow in the Yellowstone Geothermal System, Wyoming. J. Volcanol. Geotherm. Res. 123 (3–4), https://www.osti.gov/biblio/861545%20Journal%20Name:%20Journal%20of%20Volcanology%20and%20Geothermal%20Research%20Journal%20Issue:%203-4%20Journal%20Volume:%20123.

Donoghue, S.L., Neall, V.E., 2001. Late Quaternary constructional history of the southeastern Ruapehu ring plain, New Zealand. N. Z. J. Geol. Geophys. (ISSN: 11758791) 44 (3), 439–466. http://dx.doi.org/10.1080/00288306.2001.9514949.

Douglas, A., Kereszturi, G., Schaefer, L.N., Kennedy, B., 2022. Rock alteration mapping in and around fossil shallow intrusions at Mt. Ruapehu New Zealand with laboratory and aerial hyperspectral imaging. J. Volcanol. Geotherm. Res. (ISSN: 03770273) 432, http://dx.doi.org/10.1016/j.jvolgeores.2022.107700.

Ducasse, E., Adeline, K., Briottet, X., Hohmann, A., Bourguignon, A., Grandjean, G., 2020. Montmorillonite estimation in clay-quartz-calcite samples from laboratory SWIR imaging spectroscopy: A comparative study of spectral preprocessings and unmixing methods. Remote. Sens. (ISSN: 20724292) 12 (11), http://dx.doi.org/10.3390/rs12111723.

Farquharson, J.I., Wadsworth, F.B., Heap, M.J., Baud, P., 2017. Time-dependent permeability evolution in compacting volcanic fracture systems and implications for gas overpressure. J. Volcanol. Geotherm. Res. (ISSN: 03770273) 339, 81–97. http://dx.doi.org/10.1016/j.jvolgeores.2017.04.025.

Felzer, B., Hauff, P., Goetz, A.F., 1994. Quantitative reflectance spectroscopy of buddingtonite from the Cuprite mining district, Nevada. J. Geophys. Res. (ISSN: 01480227) 99 (B2), 2887–2895. http://dx.doi.org/10.1029/93JB02975.

Feng, J., Rogge, D., Rivard, B., 2018. Comparison of lithological mapping results from airborne hyperspectral VNIR-SWIR, LWIR and combined data. Int. J. Appl. Earth Obs. Geoinf. (ISSN: 1872826X) 64, 340–353. http://dx.doi.org/10.1016/j.jag.2017.03.003.

Field, C., Lombardi, G., 1972. Sulfur isotopic evidence for the supergene origin of alunite deposits, Tolfa district, Italy. Miner. Deposita (ISSN: 0026-4598) 7 (2), 113–125. http://dx.doi.org/10.1007/BF00207149, URL http://link.springer.com/10.1007/BF00207149.

Fournier, R., 1985. The behavior of silica in hydrothermal solutions. In: Berger, B.R., Bethke, P.M., Robertson, J.M. (Eds.), Geology and Geochemistry of Epithermal Systems. vol. 2, Society of Economic Geologists, pp. 45–61. http://dx.doi.org/10.5382/Rev.02.03, URL http://pubs.geoscienceworld.org/books/book/1214/chapter/107018950/The-Behavior-of-Silica-in-Hydrothermal-Solutions.

Fulignati, P., 2020. Clay minerals in hydrothermal systems. Minerals (ISSN: 2075-163X) 10 (10), 919. http://dx.doi.org/10.3390/min10100919, URL https://www.mdpi.com/2075-163X/10/10/919.

Fulignati, P., Sbrana, A., 1998. Presence of native gold and tellurium in the active high-sulfidation hydrothermal system of the La Fossa volcano (Vulcano, Italy). J. Volcanol. Geotherm. Res. (ISSN: 0377-0273) 86 (1–4), 187–198. http://dx.doi.org/10.1016/S0377-0273(98)00078-X.

Giggenbach, W.F., 1984. Mass transfer in hydrothermal alteration systems—A conceptual approach. Geochim. Cosmochim. Acta (ISSN: 00167037) 48 (12), 2693–2711. http://dx.doi.org/10.1016/0016-7037(84)90317-X, URL https://linkinghub.elsevier.com/retrieve/pii/001670378490317X.

Giggenbach, W., 1987. Redox processes governing the chemistry of fumarolic gas discharges from White Island, New Zealand. Appl. Geochem. (ISSN: 08832927) 2 (2), 143–161. http://dx.doi.org/10.1016/0883-2927(87)90030-8, URL https://linkinghub.elsevier.com/retrieve/pii/0883292787900308.

Giggenbach, W.F., 1997. The origin and evolution of fluids in magmatic-hydrothermal systems. In: Barnes, H.L. (Ed.), Geochemistry of Hydrothermal Ore Deposits. John. Wiley and Sons Inc, New York, pp. 737–796.

GNS Science, 1954. GeoNet aotearoa New Zealand manually collected volcano data. http://dx.doi.org/10.21420/PSP7-KW60.

Goetz, A.F., 2009. Three decades of hyperspectral remote sensing of the Earth: A personal view. Remote Sens. Environ. (ISSN: 0034-4257) 113 (SUPPL. 1), S5–S16. http://dx.doi.org/10.1016/J.RSE.2007.12.014.

Golden Software, 2025. Surfer. URL https://www.goldensoftware.com/products/surfer/.

Green, A., Berman, M., Switzer, P., Craig, M., 1988. A transformation for ordering multispectral data in terms of image quality with implications for noise removal. IEEE Trans. Geosci. Remote Sens. (ISSN: 01962892) 26 (1), 65–74. http://dx.doi.org/10.1109/36.3001, URL http://ieeexplore.ieee.org/document/3001/.

Heap, M.J., Baumann, T.S., Rosas-Carbajal, M., Komorowski, J.C., Gilg, H.A., Villeneuve, M., Moretti, R., Baud, P., Carbillet, L., Harnett, C., Reuschlé, T., 2021. Alteration-induced volcano instability at La Soufrière de Guadeloupe (Eastern Caribbean). J. Geophys. Res.: Solid Earth (ISSN: 21699356) 126 (8), http://dx.doi.org/10.1029/2021JB022514.

Heap, M.J., Gravley, D.M., Kennedy, B.M., Gilg, H.A., Bertolett, E., Barker, S.L., 2020. Quantifying the role of hydrothermal alteration in creating geothermal and epithermal mineral resources: The Ohakuri ignimbrite (Taupō Volcanic Zone, New Zealand). J. Volcanol. Geotherm. Res. (ISSN: 03770273) 390, http://dx.doi.org/10.1016/j.jvolgeores.2019.106703.

Heap, M.J., Troll, V.R., Kushnir, A.R., Gilg, H.A., Collinson, A.S., Deegan, F.M., Darmawan, H., Seraphine, N., Neuberg, J., Walter, T.R., 2019. Hydrothermal alteration of andesitic lava domes can lead to explosive volcanic behaviour. Nat. Commun. (ISSN: 20411723) 10 (1), http://dx.doi.org/10.1038/s41467-019-13102-8.

Hedenquist, J., 2000. Exploration for Epithermal Gold Deposits. In: Gold in 2000. Society of Economic Geologists, pp. 245–277. http://dx.doi.org/10.5382/Rev.13.07, URL http://pubs.geoscienceworld.org/books/book/1223/chapter/107026474/Exploration-for-Epithermal-Gold-Deposits.

Hedenquist, J.W., Arribas, A., 2022. Exploration implications of multiple formation environments of advanced argillic minerals. Econ. Geol. (ISSN: 15540774) 117 (3), 609–643. http://dx.doi.org/10.5382/econgeo.4880.

Heise, W., Bannister, S., Williams, C.A., McGavin, P., Caldwell, T.G., Bertrand, E.A., Usui, Y., Kilgour, G., 2024. Magmatic priming of a phreatic eruption sequence: the 2012 Te Maari eruptions at Mt Tongariro (New Zealand) imaged by magnetotellurics and seismicity. Geophys. J. Int. (ISSN: 0956-540X) 236 (3), 1848–1862. http://dx.doi.org/10.1093/gji/ggae022, URL https://academic.oup.com/gji/article/236/3/1848/7585896.

Henley, R., Ellis, A., 1983. Geothermal systems ancient and modern: a geochemical review. Earth-Sci. Rev. (ISSN: 00128252) 19 (1), 1–50. http://dx.doi.org/10.1016/0012-8252(83)90075-2, URL https://linkinghub.elsevier.com/retrieve/pii/0012825283900752.

Henley, R.W., Truesdell, A.H., Barton, P.B., Whitney, J.A., 1984. Fluid-Mineral Equilibria in Hydrothermal Systems. Society of Economic Geologists, ISBN: 0961307404, http://dx.doi.org/10.5382/Rev.01, URL https://pubs.geoscienceworld.org/segweb/books/monograph/1213/Fluid-Mineral-Equilibria-in-Hydrothermal-Systems.

Hill, G.J., Bibby, H.M., Ogawa, Y., Wallin, E.L., Bennie, S.L., Caldwell, T.G., Keys, H., Bertrand, E.A., Heise, W., 2015. Structure of the Tongariro Volcanic system: Insights from magnetotelluric imaging. Earth Planet. Sci. Lett. (ISSN: 0012821X) 432, 115–125. http://dx.doi.org/10.1016/j.epsl.2015.10.003.

Hinkle, M.E., 1991. Seasonal and geothermal production variations in concentrations of He and CO2 in soil gases, Roosevelt Hot Springs Known Geothermal Resource Area, Utah, U.S.A.. Appl. Geochem. (ISSN: 08832927) 6 (1), 35–47. http://dx.doi.org/10.1016/0883-2927(91)90061-S, URL https://linkinghub.elsevier.com/retrieve/pii/088329279190061S.

Hobden, B.J., 1997. Modelling Magmatic Trends in Time and Space: Eruptive and Magmatic History of Tongariro Volcanic Complex, New Zealand (Ph.D. thesis). University of Canterbury.

Imura, T., Ohba, T., Takahashi, R., Manalo, P., Sato, H., Ban, M., Hirata, A., Álvarez-Valero, A.M., 2024. Sulfur isotopic variations in the products of the 1895 CE eruption at Zao volcano (NE Japan): Implications for connecting eruption source and syn-eruptive magmatic-hydrothermal processes. J. Volcanol. Geotherm. Res. (ISSN: 03770273) 452, http://dx.doi.org/10.1016/j.jvolgeores.2024.108127.

John, D.A., Lee, R.G., Breit, G.N., Dilles, J.H., Calvert, A.T., Patrick Muffler, L.J., Clynne, M.A., 2019. Pleistocene hydrothermal activity on Brokeoff volcano and in the Maidu volcanic center, Lassen Peak area, northeast California: Evolution of magmatic-hydrothermal systems on stratovolcanoes. Geosphere (ISSN: 1553040X) 15 (3), 946–982. http://dx.doi.org/10.1130/GES02049.1.

John, D.A., Sisson, T.W., Breit, G.N., Rye, R.O., Vallance, J.W., 2008. Characteristics, extent and origin of hydrothermal alteration at Mount Rainier Volcano, Cascades Arc, USA: Implications for debris-flow hazards and mineral deposits. J. Volcanol. Geotherm. Res. (ISSN: 03770273) 175 (3), 289–314. http://dx.doi.org/10.1016/j.jvolgeores.2008.04.004.

Jolly, G.E., Keys, H.J., Procter, J.N., Deligne, N.I., 2014. Overview of the co-ordinated risk-based approach to science and management response and recovery for the 2012 eruptions of Tongariro volcano, New Zealand. J. Volcanol. Geotherm. Res. (ISSN: 03770273) 286, 184–207. http://dx.doi.org/10.1016/j.jvolgeores.2014.08.028.

Keigler, R., Thouret, J.C., Hodgson, K.A., Neall, V.E., Lecointre, J.A., Procter, J.N., Cronin, S.J., 2011. The Whangaehu Formation: Debris-avalanche and lahar deposits from ancestral Ruapehu volcano, New Zealand. Geomorphology (ISSN: 0169555X) 133 (1–2), 57–79. http://dx.doi.org/10.1016/j.geomorph.2011.06.019.

Kereszturi, G., Heap, M., Schaefer, L.N., Darmawan, H., Deegan, F.M., Kennedy, B., Komorowski, J.C., Mead, S., Rosas-Carbajal, M., Ryan, A., Troll, V.R., Villeneuve, M., Walter, T.R., 2023. Porosity, strength, and alteration – Towards a new volcano stability assessment tool using VNIR-SWIR reflectance spectroscopy. Earth Planet. Sci. Lett. (ISSN: 0012821X) 602, http://dx.doi.org/10.1016/j.epsl.2022.117929.

Kereszturi, G., Schaefer, L., Mead, S., Miller, C., Procter, J., Kennedy, B., 2021. Synthesis of hydrothermal alteration, rock mechanics and geophysical mapping to constrain failure and debris avalanche hazards at Mt. Ruapehu (New Zealand). N. Z. J. Geol. Geophys. (ISSN: 11758791) 64 (2–3), 421–442. http://dx.doi.org/10.1080/00288306.2021.1885048.

Kereszturi, G., Schaefer, L.N., Miller, C., Mead, S., 2020. Hydrothermal alteration on composite volcanoes: Mineralogy, hyperspectral imaging, and aeromagnetic study of Mt Ruapehu, New Zealand. Geochem. Geophys. Geosystems (ISSN: 15252027) 21 (9), http://dx.doi.org/10.1029/2020GC009270.

Kereszturi, G., Schaefer, L.N., Schleiffarth, W.K., Procter, J., Pullanagari, R.R., Mead, S., Kennedy, B., 2018. Integrating airborne hyperspectral imagery and LiDAR for volcano mapping and monitoring through image classification. Int. J. Appl. Earth Obs. Geoinf. (ISSN: 1872826X) 73, 323–339. http://dx.doi.org/10.1016/j.jag.2018.07.006.

Kilgour, G., Kennedy, B., Scott, B., Christenson, B., Jolly, A., Asher, C., Rosenberg, M., Saunders, K., 2021. Whakaari/White Island: a review of New Zealand's most active volcano. N. Z. J. Geol. Geophys. (ISSN: 11758791) 64 (2–3), 273–295. http://dx.doi.org/10.1080/00288306.2021.1918186.

Kilgour, G., Manville, V., Pasqua, F.D., Graettinger, A., Hodgson, K.A., Jolly, G.E., 2010. The 25 September 2007 eruption of Mount Ruapehu, New Zealand: Directed ballistics, surtseyan jets, and ice-slurry lahars. J. Volcanol. Geotherm. Res. (ISSN: 03770273) 191 (1–2), 1–14. http://dx.doi.org/10.1016/j.jvolgeores.2009.10.015.

Klammer, D., 1997. Mass change during extreme acid-sulphate hydrothermal alteration of a Tertiary latite, Styria, Austria. Chem. Geol. (ISSN: 00092541) 141 (1–2), 33–48. http://dx.doi.org/10.1016/S0009-2541(97)00056-9, URL https://linkinghub.elsevier.com/retrieve/pii/S0009254197000569.

Kokaly, R.F., Clark, R.N., Swayze, G.A., Livo, K.E., Hoefen, T.M., Pearson, N.C., Wise, R.A., Benzel, W., Lowers, H.A., Driscoll, R.L., Klein, A.J., Survey, U.S.G., 2017. USGS spectral library version 7. In: Data Series. Reston, VA, p. 68. http://dx.doi.org/10.3133/ds1035, URL https://pubs.usgs.gov/publication/ds1035.

Kumar, V., Ghosh, J.K., 2017. Camouflage detection using MWIR hyperspectral images. J. the Indian Soc. Remote. Sens. (ISSN: 09743006) 45 (1), 139–145. http://dx.doi.org/10.1007/s12524-016-0555-8.

Lecointre, J.A., Neall, V.E., Palmer, A.S., 1998. Quaternary lahar stratigraphy of the western Ruapehu ring plain, New Zealand. N. Z. J. Geol. Geophys. (ISSN: 11758791) 41 (3), 225–245. http://dx.doi.org/10.1080/00288306.1998.9514807.

Lecointre, J.A., Neall, V.E., Wallace, C.R., Prebble, W.M., 2002. The 55- to 60-ka Te Whaiau formation: A catastrophic, avalanche-induced, cohesive debris-flow deposit from Proto-Tongariro volcano, New Zealand. Bull. Volcanol. (ISSN: 02588900) 63 (8), 509–525. http://dx.doi.org/10.1007/s004450100167.

Leonard, G.S., Cole, R.P., Christenson, B.W., Conway, C.E., Cronin, S.J., Gamble, J.A., Hurst, T., Kennedy, B.M., Miller, C.A., Procter, J.N., Pure, L.R., Townsend, D.B., White, J.D., Wilson, C.J., 2021. Ruapehu and Tongariro stratovolcanoes: a review of current understanding. N. Z. J. Geol. Geophys. (ISSN: 11758791) 64 (2–3), 389–420. http://dx.doi.org/10.1080/00288306.2021.1909080.

Li, B., Wiedenbeck, M., Couffignal, F., Álvarez-Valero, A.M., Bao, H.-M., Fan, C.-F., Han, J., Jin, G.-S., Peng, Y.-B., Syczewski, M.D., Tait, K.T., Wilke, F.D., Wortmann, U.G., 2024. Barite, anhydrite and gypsum reference materials for in situ oxygen and sulfur isotope ratio measurements. Geostand. Geoanalytical Res. (ISSN: 1639-4488) 48 (1), 179–205. http://dx.doi.org/10.1111/ggr.12533, URL https://onlinelibrary.wiley.com/doi/10.1111/ggr.12533.

Liu, C., Frazier, P., Kumar, L., 2007. Comparative assessment of the measures of thematic classification accuracy. Remote Sens. Environ. (ISSN: 00344257) 107 (4), 606–616. http://dx.doi.org/10.1016/j.rse.2006.10.010.

Lorenzo, A., García-Vicente, A., Morales, J., García-Romero, E., Suárez, M., 2021. Spectral response (VNIR-swir) associated with the octahedral sheet of smectites. In: The 2nd International Electronic Conference on Mineral Science. MDPI, Basel Switzerland, p. 23. http://dx.doi.org/10.3390/iecms2021-09352, URL https://www.mdpi.com/2673-4931/6/1/23.

Lowenstern, J.B., 2001. Carbon dioxide in magmas and implications for hydrothermal systems. Miner. Deposita (ISSN: 00264598) 36 (6), 490–502. http://dx.doi.org/10.1007/s001260100185.

Luhmann, A.J., Tutolo, B.M., Bagley, B.C., Mildner, D.F., Seyfried, W.E., Saar, M.O., 2017. Permeability, porosity, and mineral surface area changes in basalt cores induced by reactive transport of CO2-rich brine. Water Resour. Res. (ISSN: 19447973) 53 (3), 1908–1927. http://dx.doi.org/10.1002/2016WR019216.

Manalo, P.C., Imai, A., Subang, L.L., de los Santos, M.C., Yanagi, K., Takahashi, R., Blamey, N.J.F., 2018. Mineralization of the northwest quartz-pyrite-gold veins: Implications for multiple mineralization events at Lepanto, Mankayan Mineral District, Northern Luzon, Philippines. Econ. Geol. (ISSN: 0361-0128) 113 (7), 1609–1626. http://dx.doi.org/10.5382/econgeo.2018.4606.

Mayer, K., Scheu, B., Montanaro, C., Yilmaz, T.I., Isaia, R., Aßbichler, D., Dingwell, D.B., 2016. Hydrothermal alteration of surficial rocks at Solfatara (Campi Flegrei): Petrophysical properties and implications for phreatic eruption processes. J. Volcanol. Geotherm. Res. (ISSN: 03770273) 320, 128–143. http://dx.doi.org/10.1016/j.jvolgeores.2016.04.020.

Mayer, K., Scheu, B., Yilmaz, T.I., Montanaro, C., Albert Gilg, H., Rott, S., Joseph, E.P., Dingwell, D.B., 2017. Phreatic activity and hydrothermal alteration in the Valley of Desolation, Dominica, Lesser Antilles. Bull. Volcanol. (ISSN: 14320819) 79 (12), http://dx.doi.org/10.1007/s00445-017-1166-0.

Mazot, A., Bernard, A., Fischer, T., Inguaggiato, S., Sutawidjaja, I.S., 2008. Chemical evolution of thermal waters and changes in the hydrothermal system of Papandayan volcano (West Java, Indonesia) after the November 2002 eruption. J. Volcanol. Geotherm. Res. (ISSN: 03770273) 178 (2), 276–286. http://dx.doi.org/10.1016/j.jvolgeores.2008.06.022.

McCollom, T.M., Shock, E.L., 1998. Fluid-rock interactions in the lower oceanic crust: Thermodynamic models of hydrothermal alteration. J. Geophys. Res.: Solid Earth (ISSN: 21699356) 103 (1), 547–575. http://dx.doi.org/10.1029/97jb02603.

Meyer, C., Hemley, J.J., 1967. Wall Rock Alteration. In: Barnes, H.L. (Ed.), Geochemistry of Hydrothermal Ore Deposits. Holt, Rinehart and Winston, New York, pp. 166–235.

Mick, E., Stix, J., de Moor, J.M., Avard, G., 2021. Hydrothermal alteration and sealing at Turrialba volcano, Costa Rica, as a mechanism for phreatic eruption triggering. J. Volcanol. Geotherm. Res. (ISSN: 03770273) 416, http://dx.doi.org/10.1016/j.jvolgeores.2021.107297.

Milewski, R., Chabrillat, S., Brell, M., Schleicher, A.M., Guanter, L., 2019. Assessment of the 1.75 μm absorption feature for gypsum estimation using laboratory, air- and spaceborne hyperspectral sensors. Int. J. Appl. Earth Obs. Geoinf. (ISSN: 1872826X) 77, 69–83. http://dx.doi.org/10.1016/j.jag.2018.12.012.

Miller, C.A., Christenson, B.W., Byrdina, S., Vandemeulebrouck, J., Brakenrig, T., Britten, K., Shanks, J., Epstein, G., 2020. Snapshot of a magmatic/hydrothermal system from electrical resistivity tomography and fumarolic composition, Whakaari/White Island, New Zealand. J. Volcanol. Geotherm. Res. (ISSN: 03770273) 400, http://dx.doi.org/10.1016/j.jvolgeores.2020.106909.

Miller, J.L., Elwood Madden, A.S., Phillips-Lander, C.M., Pritchett, B.N., Elwood Madden, M.E., 2016. Alunite dissolution rates: Dissolution mechanisms and implications for Mars. Geochim. Cosmochim. Acta (ISSN: 00167037) 172, 93–106. http://dx.doi.org/10.1016/j.gca.2015.10.001.

Miller, C.A., Kang, S.G., Fournier, D., Hill, G., 2018. Distribution of vapor and condensate in a hydrothermal system: Insights from self-potential inversion at Mount Tongariro, New Zealand. Geophys. Res. Lett. (ISSN: 19448007) 45 (16), 8190–8198. http://dx.doi.org/10.1029/2018GL078780.

Miller, C.A., Williams-Jones, G., 2016. Internal structure and volcanic hazard potential of Mt Tongariro, New Zealand, from 3D gravity and magnetic models. J. Volcanol. Geotherm. Res. (ISSN: 03770273) 319, 12–28. http://dx.doi.org/10.1016/j.jvolgeores.2016.03.012.

Milliken, R.E., Swayze, G.A., Arvidson, R.E., Bishop, J.L., Clark, R.N., Ehlmann, B.L., Green, R.O., Grotzinger, J.P., Morris, R.V., Murchie, S.L., Mustard, J.F., Weitz, C., 2008. Opaline silica in young deposits on Mars. Geology (ISSN: 00917613) 36 (11), 847–850. http://dx.doi.org/10.1130/G24967A.1.

Moebis, A., Cronin, S.J., Neall, V.E., Smith, I.E., 2011. Unravelling a complex volcanic history from fine-grained, intricate Holocene ash sequences at the Tongariro Volcanic Centre, New Zealand. Quat. Int. (ISSN: 10406182) 246 (1–2), 352–363. http://dx.doi.org/10.1016/j.quaint.2011.05.035.

Montanaro, C., Cronin, S., Scheu, B., Kennedy, B., Scott, B., 2020. Complex crater fields formed by steam-driven eruptions: Lake Okaro, New Zealand. Bull. Geol. Soc. Am. (ISSN: 19432674) 132 (9–10), 1914–1930. http://dx.doi.org/10.1130/B35276.1.

Montanaro, C., Mick, E., Salas-Navarro, J., Caudron, C., Cronin, S.J., de Moor, J.M., Scheu, B., Stix, J., Strehlow, K., 2022. Phreatic and hydrothermal eruptions: From overlooked to looking over. Bull. Volcanol. (ISSN: 14320819) 84 (6), http://dx.doi.org/10.1007/s00445-022-01571-7.

Mordensky, S.P., Heap, M.J., Kennedy, B.M., Gilg, H.A., Villeneuve, M.C., Farquharson, J.I., Gravley, D.M., 2019. Influence of alteration on the mechanical behaviour and failure mode of andesite: implications for shallow seismicity and volcano monitoring. Bull. Volcanol. (ISSN: 14320819) 81 (8), http://dx.doi.org/10.1007/s00445-019-1306-9.

Mueller, S., Melnik, O., Spieler, O., Scheu, B., Dingwell, D.B., 2005. Permeability and degassing of dome lavas undergoing rapid decompression: An experimental determination. Bull. Volcanol. (ISSN: 02588900) 67 (6), 526–538. http://dx.doi.org/10.1007/s00445-004-0392-4.

Pacey, A., Wilkinson, J.J., Boyce, A.J., Millar, I.L., 2020. Magmatic fluids implicated in the formation of propylitic alteration: Oxygen, hydrogen, and strontium isotope constraints from the northparkes porphyry Cu-Au district, New South Wales, Australia. Econ. Geol. (ISSN: 0361-0128) 115 (4), 729–748. http://dx.doi.org/10.5382/ECONGEO.4732.

Pal, M., 2005. Random forest classifier for remote sensing classification. Int. J. Remote Sens. (ISSN: 01431161) 26 (1), 217–222. http://dx.doi.org/10.1080/01431160412331269698.

Pardo, N., Cronin, S.J., Németh, K., Brenna, M., Schipper, C.I., Breard, E., White, J.D., Procter, J., Stewart, B., Agustín-Flores, J., Moebis, A., Zernack, A., Kereszturi, G., Lube, G., Auer, A., Neall, V., Wallace, C., 2014. Perils in distinguishing phreatic from phreatomagmatic ash; insights into the eruption mechanisms of the 6 August 2012 Mt. Tongariro eruption, New Zealand. J. Volcanol. Geotherm. Res. (ISSN: 03770273) 286, 397–414. http://dx.doi.org/10.1016/j.jvolgeores.2014.05.001.

Philipp, S.L., 2021. Fracture systems and fluid flow in geothermal reservoirs. In: World Geothermal Congress 2020+1. Reykjavik.

Pirajno, F., 1992. Hydrothermal Mineral Deposits. Springer Berlin Heidelberg, Berlin, Heidelberg, ISBN: 978-3-642-75673-3, http://dx.doi.org/10.1007/978-3-642-75671-9, URL https://link.springer.com/10.1007/978-3-642-75671-9.

Plaza, A., Benediktsson, J.A., Boardman, J.W., Brazile, J., Bruzzone, L., Camps-Valls, G., Chanussot, J., Fauvel, M., Gamba, P., Gualtieri, A., Marconcini, M., Tilton, J.C., Trianni, G., 2009. Recent advances in techniques for hyperspectral image processing. Remote Sens. Environ. (ISSN: 0034-4257) 113 (SUPPL. 1), S110–S122. http://dx.doi.org/10.1016/J.RSE.2007.07.028.

Potro, R.d., Hürlimann, M., 2009. The decrease in the shear strength of volcanic materials with argillic hydrothermal alteration, insights from the summit region of Teide stratovolcano, Tenerife. Eng. Geol. (ISSN: 00137952) 104 (1–2), 135–143. http://dx.doi.org/10.1016/j.enggeo.2008.09.005.

Pour, A.B., Hashim, M., 2012. Identifying areas of high economic-potential copper mineralization using ASTER data in the Urumieh-Dokhtar Volcanic Belt, Iran. Adv. Space Res. (ISSN: 02731177) 49 (4), 753–769. http://dx.doi.org/10.1016/j.asr.2011.11.028.

Procter, J.N., Cronin, S.J., Zernack, A.V., Lube, G., Stewart, R.B., Nemeth, K., Keys, H., 2014. Debris flow evolution and the activation of an explosive hydrothermal system; Te Maari, Tongariro, New Zealand. J. Volcanol. Geotherm. Res. (ISSN: 03770273) 286, 303–316. http://dx.doi.org/10.1016/j.jvolgeores.2014.07.006.

Pure, L.R., Leonard, G.S., Townsend, D.B., Wilson, C.J., Calvert, A.T., Cole, R.P., Conway, C.E., Gamble, J.A., Smith, T.B., 2020. A high resolution 40Ar/39Ar lava chronology and edifice construction history for Tongariro volcano, New Zealand. J. Volcanol. Geotherm. Res. (ISSN: 03770273) 403, http://dx.doi.org/10.1016/j.jvolgeores.2020.106993.

Pure, L.R., Wilson, C.J., Charlier, B.L., Gamble, J.A., Townsend, D.B., Leonard, G.S., 2023. The compositional diversity and temporal evolution of an active andesitic arc stratovolcano: Tongariro, Taupō Volcanic Zone, New Zealand. Contrib. Miner. Pet. (ISSN: 14320967) 178 (5), http://dx.doi.org/10.1007/s00410-023-02004-0.

Rafter, A., 1957. Sulphur isotopic variation in nature, part 1. The preparation of sulphur dioxide for mass spectrometer examination. N. Z. J. Sci. Tech. B 38, 849, URL https://cir.nii.ac.jp/crid/1571698599637353600.bib?lang=en.

Rees, C.E., Holt, B.D., 1991. The isotopic analysis of sulphur and oxygen. In: Stable Isotopes: Natural and Anthropogenic Sulphur in the Environment. John Wiley and Sons, Chichester, ISBN: 0-471-92646-9, pp. 43–64.

Reid, M.E., Sisson, T.W., Brien, D.L., 2001. Volcano collapse promoted by hydrothermal alteration and edifice shape, Mount Rainier, Washington. Geology (ISSN: 0091-7613) 29 (9), 779. http://dx.doi.org/10.1130/0091-7613(2001)029<0779:VCPBHA>2.0.CO;2, URL https://pubs.geoscienceworld.org/geology/article/29/9/779-782/191790.

Richter, R., Schläpfer, D., 2002. Geo-atmospheric processing of airborne imaging spectrometry data. Part 2: Atmospheric/topographic correction. Int. J. Remote Sens. (ISSN: 01431161) 23 (13), 2631–2649. http://dx.doi.org/10.1080/01431160110115834.

Richter, R., Schläpfer, D., 2023. Atmospheric / Topographic Correction for Airborne Imagery (ATCOR-4 User Guide, Version 7.5., August 2023). Tech. rep., URL https://www.rese-apps.com/pdf/atcor4_manual.pdf.

Robinson, B.W., Kusakabe, M., 1975. Quantitative preparation of sulfur dioxide, for sulfur-34/sulfur-32 analyses, from sulfides by combustion with cuprous oxide. Anal. Chem. 47 (7), 1179–1181.

Rodgers, K.A., Cook, K.L., Browne, P.R.L., Campbell, K.A., 2002. The mineralogy, texture and significance of silica derived from alteration by steam condensate in three New Zealand geothermal fields. Clay Miner. (ISSN: 0009-8558) 37 (2), 299–322. http://dx.doi.org/10.1180/0009855023720035.

Rodriguez-Gomez, C., Kereszturi, G., Reeves, R., Rae, A., Pullanagari, R., Jeyakumar, P., Procter, J., 2021. Lithological mapping of Waiotapu Geothermal Field (New Zealand) using hyperspectral and thermal remote sensing and ground exploration techniques. Geothermics (ISSN: 03756505) 96, http://dx.doi.org/10.1016/j.geothermics.2021.102195.

Rowe, G.L., Brantley, S.L., Fernandez, M., Fernandez, J.F., Borgia, A., Barquero, J., 1992. Fluid-volcano interaction in an active stratovolcano: the crater lake system of Poás volcano, Costa Rica. J. Volcanol. Geotherm. Res. (ISSN: 03770273) 49 (1–2), 23–51. http://dx.doi.org/10.1016/0377-0273(92)90003-V, URL https://linkinghub.elsevier.com/retrieve/pii/037702739290003V.

Rowland, J.V., Simmons, S.F., 2012. Hydrologic, magmatic, and tectonic controls on hydrothermal flow, Taupo Volcanic Zone, New Zealand: Implications for the formation of epithermal vein deposits. Econ. Geol. (ISSN: 0361-0128) 107 (3), 427–457. http://dx.doi.org/10.2113/econgeo.107.3.427.

Rye, R.O., 2005. A review of the stable-isotope geochemistry of sulfate minerals in selected igneous environments and related hydrothermal systems. Chem. Geol. (ISSN: 00092541) 215 (1-4 SPEC. ISS.), 5–36. http://dx.doi.org/10.1016/j.chemgeo.2004.06.034.

Rye, R.O., Alpers, C.N., 1997. The Stable Isotope Geochemistry of Jarosite. Tech. Rep., U.S. Geological Survey.

Rye, R.O., Bethke, P.M., Wasserman, M.D., 1992. The stable isotope geochemistry of acid sulfate alteration. Econ. Geol. (ISSN: 1554-0774) 87 (2), 225–262. http://dx.doi.org/10.2113/gsecongeo.87.2.225, URL http://pubs.geoscienceworld.org/economicgeology/article/87/2/225/21006/The-stable-isotope-geochemistry-of-acid-sulfate.

Sanchez, R., Kereszturi, G., Álverez-Valero, A., Suárez, M., Kilgour, G., Zellmer, G., 2025. Timescales and processes of hydrothermal alteration at Te Maari Tongariro, New Zealand: Insights utilizing petrographic and mass balance techniques. http://dx.doi.org/10.2139/ssrn.5690358, Available at SSRN: URL https://www.ssrn.com/abstract=5690358.

Santamaría-López, Á., Suárez, M., García-Romero, E., 2024. Detection limits of kaolinites and some common minerals in binary mixtures by short-wave infrared spectroscopy. Appl. Clay Sci. (ISSN: 01691317) 250, http://dx.doi.org/10.1016/j.clay.2024.107269.

Schwartz, G.M., 1959. Hydrothermal alteration. Econ. Geol. (ISSN: 1554-0774) 54 (2), 161–183. http://dx.doi.org/10.2113/gsecongeo.54.2.161, URL http://pubs.geoscienceworld.org/economicgeology/article/54/2/161/16741/Hydrothermal-alteration.

Scott, B.J., Potter, S.H., 2014. Aspects of historical eruptive activity and volcanic unrest at Mt. Tongariro, New Zealand: 1846-2013. J. Volcanol. Geotherm. Res. (ISSN: 03770273) 286, 263–276. http://dx.doi.org/10.1016/j.jvolgeores.2014.04.003.

Seal, R.R., Alpers, C.N., Rye, R.O., 2000. Stable isotope systematics of sulfate minerals. Rev. Miner. Geochem. (ISSN: 1529-6466) 40 (1), 541–602. http://dx.doi.org/10.2138/rmg.2000.40.12, URL https://pubs.geoscienceworld.org/rimg/article/40/1/541-602/140672.

Shane, P., Maas, R., Lindsay, J., 2017. History of Red Crater volcano, Tongariro Volcanic Centre (New Zealand): Abrupt shift in magmatism following recharge and contrasting evolution between neighboring volcanoes. J. Volcanol. Geotherm. Res. (ISSN: 03770273) 340, 1–15. http://dx.doi.org/10.1016/j.jvolgeores.2017.04.008.

Sichel, H., 1966. The estimation of means and associated confidence limits for small samples from lognormal populations. In: 1996 Symp. South African Institute of Mining and Metallurgy.

Simons, B.C., 2014. Volcanic History and Eruption Processes of Blue Lake Crater, Tongariro (Ph.D. thesis). University of Waikato.

Simpson, M.P., Rae, A.J., 2018. Short-wave infrared (SWIR) reflectance spectrometric characterisation of clays from geothermal systems of the Taupō Volcanic Zone, New Zealand. Geothermics (ISSN: 03756505) 73, 74–90. http://dx.doi.org/10.1016/j.geothermics.2018.01.006.

Sinclair, A., 1974. Selection of threshold values in geochemical data using probability graphs. J. Geochem. Explor. (ISSN: 03756742) 3 (2), 129–149. http://dx.doi.org/10.1016/0375-6742(74)90030-2, URL https://linkinghub.elsevier.com/retrieve/pii/0375674274900302.

Stevens, N.F., 2002. Emplacement of the large andesite lava flow in the Oturere Stream valley, Tongariro Volcano, from airborne interferometric radar. N. Z. J. Geol. Geophys. (ISSN: 11758791) 45 (3), 387–394. http://dx.doi.org/10.1080/00288306.2002.9514980.

Stoffregen, R.E., 1987. Genesis of acid-sulfate alteration and Au-Cu-Ag mineralization at Summitville, Colorado. Econ. Geol. (ISSN: 0361-0128) 82 (6), 1575–1591. http://dx.doi.org/10.2113/gsecongeo.82.6.1575.

Stoffregen, R.E., 1993. Stability relations of jarosite and natrojarosite at 150–250°C. Geochim. Cosmochim. Acta (ISSN: 00167037) 57 (11), 2417–2429. http://dx.doi.org/10.1016/0016-7037(93)90406-M, URL https://linkinghub.elsevier.com/retrieve/pii/001670379390406M.

Stoffregen, R.E., Alpers, C.N., Jambor, J.L., 2000. Alunite-jarosite crystallography, thermodynamics, and geochronology. Rev. Miner. Geochem. (ISSN: 1529-6466) 40 (1), 453–479. http://dx.doi.org/10.2138/rmg.2000.40.9, URL https://pubs.geoscienceworld.org/rimg/article/40/1/453-479/140669.

Story, M., Congalton, R.G., 1986. Accuracy assessment: a user's perspective. Photogramm. Eng. Remote Sens. 52 (3), 397–399.

Symonds, R., Gerlach, T., Reed, M., 2001. Magmatic gas scrubbing: implications for volcano monitoring. J. Volcanol. Geotherm. Res. (ISSN: 03770273) 108 (1–4), 303–341. http://dx.doi.org/10.1016/S0377-0273(00)00292-4, URL https://linkinghub.elsevier.com/retrieve/pii/S0377027300002924.

Taran, Y., Carlos Gavilanes, J., Cortes, A., Aurora Armienta, M., 2000. Chemical precursors to the 1998–1999 eruption of Colima Volcano, Mexico. Rev. Mex. de Cienc. Geológicas 17 (2), 111–124.

Thiele, S.T., Kereszturi, G., Heap, M.J., Ribeiro, A.d., Kamath, A., Kidd, M., Tramontini, M., Rosas-Carbajal, M., Gloaguen, R., 2025. Hyperspectral mapping of density, porosity, stiffness, and strength in hydrothermally altered volcanic rocks. http://dx.doi.org/10.5194/egusphere-2025-1904, URL https://egusphere.copernicus.org/preprints/2025/egusphere-2025-1904/.

Topping, W., 1974. Some Aspects of Quaternary History of Tongariro Volcanic Centre (Ph.D. thesis). Victoria University of Wellington, Wellington.

Tost, M., Cronin, S.J., Procter, J.N., 2014. Transport and emplacement mechanisms of channelised long-runout debris avalanches, Ruapehu volcano, New Zealand. Bull. Volcanol. (ISSN: 14320819) 76 (12), 1–14. http://dx.doi.org/10.1007/s00445-014-0881-z.

van der Meer, F., Van Der Werff, H.M., Van Ruitenbeek, F.J., Hecker, C.A., Bakker, W.H., Noomen, M.F., van der Meijde, M., Carranza, E.J.M., de Smeth, J.B., Woldai, T., 2012. Multi- and hyperspectral geologic remote sensing: A review. Int. J. Appl. Earth Obs. Geoinf. (ISSN: 1872826X) 14 (1), 112–128. http://dx.doi.org/10.1016/j.jag.2011.08.002.

Vicente, J., Mead, S., Kereszturi, G., Miller, C., 2025. Simulation of the 2012 Te Maari debris avalanche: Insight into the failure mechanics and the role of the hydrothermal system. J. Volcanol. Geotherm. Res. (ISSN: 03770273) 108351. http://dx.doi.org/10.1016/j.jvolgeores.2025.108351, URL https://linkinghub.elsevier.com/retrieve/pii/S0377027325000873.

Vikre, P.G., 1987. Paleohydrology of Buckskin Mountain, National District, Humboldt County, Nevada. Econ. Geol. (ISSN: 0361-0128) 82 (4), 934–950. http://dx.doi.org/10.2113/gsecongeo.82.4.934.

Wadsworth, F.B., Kennedy, B.M., Branney, M.J., von Aulock, F.W., Lavallée, Y., Menendez, A., 2015. Exhumed conduit records magma ascent and drain-back during a Strombolian eruption at Tongariro volcano, New Zealand. Bull. Volcanol. (ISSN: 14320819) 77 (9), http://dx.doi.org/10.1007/s00445-015-0962-7.

Walsh, F., Hochstein, M., Bromley, C., 1998. The Tongariro geothermal system (NZ): Review of geophysical data. In: Proceedings 20th Geothermal Workshop. pp. 317–324.

Wasserman, M.D., Rye, R.O., Bethke, P.M., Arribas, A., 1992. Methods for Separation and Total Stable Isotope Analysis of Alunite. Tech. Rep., U.S. Geological Survey, URL https://pubs.er.usgs.gov/ublication/ofr929.

West Systems, 2019. Portable Diffuse Flux Meter Handbook, Release 9.1. Tech. Rep.

Williams-Jones, G., Stix, J., Heiligmann, M., Charland, A., Sherwood Lollar, B., Arner, N., Garzón, G.V., Barquero, J., Fernandez, E., 2000. A model of diffuse degassing at three subduction-related volcanoes. Bull. Volcanol. (ISSN: 0258-8900) 62 (2), 130–142. http://dx.doi.org/10.1007/s004450000075, URL http://link.springer.com/10.1007/s004450000075.

Wilson, C.J.N., Houghton, B.F., Mcwilliams, M.O., Lanphere, M.A., Weaver, S.D., Briggs, R.M., 1995. Volcanic and structural evolution of Taupo Volcanic Zone, New Zealand: a review. J. Volcanol. Geotherm. Res. 68, 1–28.

Wright, H.M., Cashman, K.V., Gottesfeld, E.H., Roberts, J.J., 2009. Pore structure of volcanic clasts: Measurements of permeability and electrical conductivity. Earth Planet. Sci. Lett. (ISSN: 0012821X) 280 (1–4), 93–104. http://dx.doi.org/10.1016/j.epsl.2009.01.023.

Xu, T., Pruess, K., 2001. On fluid flow and mineral alteration in fractured caprock of magmatic hydrothermal systems. J. Geophys. Res.: Solid Earth (ISSN: 0148-0227) 106 (B2), 2121–2138. http://dx.doi.org/10.1029/2000JB900356.

Yanagisawa, F., Sakai, H., 1983. Thermal decomposition of barium sulfate-vanadium pentoxide-silica glass mixtures for preparation of sulfur dioxide in sulfur isotope ratio measurements. Anal. Chem. 55 (6), 985–987.

Yang, T.H.J., Chambefort, I., Rowe, M., Mazot, A., Seward, A., Werner, C., Fischer, T., Seastres, J., Siega, F., Macdonald, N., Brakenrig, T., Coup, L., Sander, F., 2024. Variability in surface CO2 flux: Implication for monitoring surface emission from geothermal fields. Geothermics (ISSN: 03756505) 120, http://dx.doi.org/10.1016/j.geothermics.2024.102981.

Zimbelman, D.R., Rye, R.O., Breit, G.N., 2005. Origin of secondary sulfate minerals on active andesitic stratovolcanoes. Chem. Geol. (ISSN: 00092541) 215 (1-4 SPEC. ISS.), 37–60. http://dx.doi.org/10.1016/j.chemgeo.2004.06.056.